



School of Chemistry

[Thermionic Emission Studies of n-type Semiconducting Diamond]

[Mark Lowman]

**This thesis is submitted in partial fulfilment of the requirements for the Honours
Degree of MSci (Bsc) at the University of Bristol**

[Neil Fox]

[Paul May]

[Physical and Theoretical]

Abstract

Recently, diamond-based materials have seen an increase in interest for research into electron emission applications, in particular energy conversion using thermionics, where electrical energy can be converted to thermal energy with no moving parts. The increased interest in diamond stems from the unique material property that once hydrogen-terminated it develops a negative electron affinity, and when paired with nitrogen-doping in the bulk, it forms a low work function material that is perfect as an electron emitter. Three samples were grown using microwave plasma chemical vapour deposition, a short and a long growth on thermal grade diamond, D1 and D2 respectively, and a short growth on molybdenum, Mo1. The samples were characterised via Raman spectroscopy, and a morphological investigation was carried out on the samples using scanning electron microscopy which showed very nanocrystalline surfaces on D1 and Mo1, whereas D2 showed a considerably larger grain boundary and a smoother surface. The thermionic properties of each sample were examined under high vacuum conditions, by radiatively heating each sample, and measuring the current between the emitter (sample) and a collector electrode. Generally, the thinner films had a greater emission current, which was attributed to the enhancement in conductivity gained from having denser grain boundaries. The film grown on molybdenum ubiquitously showed the highest emission currents, stemming from molybdenum being considerably more conductive than bulk diamond. The effect of an enclosed beta source, ^{63}Ni (28 MBq), was also examined. Samples D2 and Mo1 saw an increase in emission current when irradiated by beta radiation. The data obtained tended to be very unpredictable and vary under the same conditions. Some suggestions for their origins are discussed.

Acknowledgements

I would like to extend my gratitude to Gary Wan, who showed me how to use the thermionics rig and the microwave reactor. Without his guidance, I would not have been able to write this. I'd also like to give a large thank you to Ed Smith, who, even not being my supervisor, has always been there to help where he can, and generally makes the diamond lab a better place to be.

I'd like to thank my second assessor Paul May for cultivating an excellent environment down in the diamond lab. Also, my project supervisor Neil Fox, without who none of this could have been possible.

Finally, I'd like to thank the whole diamond lab for encouragement and small pointers when needed.

Table of Contents

1	Introduction.....	5
1.1	<i>Diamond</i>	5
1.1.1	Physical Properties	5
1.1.2	Electronic Properties	5
1.1.3	Synthesis	6
1.1.4	Doping and Semiconducting Diamond.....	7
1.1.5	Hydrogen Termination	9
1.1.6	Surface Morphology.....	11
1.1.7	Grain Boundaries.....	11
1.2	<i>Thermionic Emission</i>	12
1.2.1	History.....	12
1.2.2	Richardson’s Law and the Theory of Thermionic Emission.....	12
1.2.3	Beta Enhancement.....	13
1.3	<i>Thermionic Energy Converters and Other Applications for Electron Sources</i>	14
1.3.1	Thermionic Energy Converter Overview.....	14
1.3.2	Research into Thermionic Energy Converters	15
1.3.3	Diamond Emitters	16
1.3.4	Other Applications of Diamond Emitters	17
1.4	<i>Review of Work Done by the University of Bristol</i>	17
1.4.1	Growing Nitrogen Doped Diamond	17
1.4.2	Field Emission from Grain Boundaries	18
1.4.3	Variation of Work Function Across the Surface of H-terminated Diamond.....	18
2	Methodology	18
2.1	<i>Sample Growths and Preparations</i>	18
2.1.1	Apparatus	18
2.1.1	Diamond Backside Growth (Samples D1 and D2)	19
2.1.2	Diamond Substrate Growths.....	20
2.1.3	Molybdenum Substrate Growths	20

2.1.4	Plasmonic Grating (Sample Mo1)	21
2.1.5	H-Termination	21
2.2	<i>Sample Characterisation</i>	22
2.2.1	SEM	22
2.2.2	Raman Spectroscopy	22
2.3	<i>Thermionic Studies</i>	22
2.3.1	Apparatus	22
2.3.2	Thermionic Runs	24
2.3.3	Beta Enhancement	24
3	Results and Discussion	25
3.1	<i>Characterisation</i>	25
3.1.1	Raman Spectroscopy	25
3.1.2	SEM Data	26
3.2	<i>Thermionics Data</i>	28
3.2.1	Results	28
3.2.3	Effect of Substrate on Thermionic Emission	36
3.2.4	Notes on Results and Potential Improvements to the Method	37
4	Conclusion	39
5	Further Work	40
6	Bibliography	41

1 Introduction

1.1 Diamond

1.1.1 Physical Properties

Diamond is one of carbon's two crystalline allotropes, comprised of tetrahedral sp^3 hybridised carbon atoms packed into a cubic or hexagonal structure. The strength of these bonds results in diamond being the densest material known to man (3.515 g cm^{-3}), as well as being an outstanding thermal conductor^[1]. It is no surprise then that diamonds have seen applications utilising these physical characteristics, from the tips of drill bits, saw blades, even as surgical scalpels^[2].

The Gibbs free energy change of the oxidation of diamond to graphite is $\sim -3 \text{ kJ mol}^{-1}$ at 298 K, thus being a thermodynamically favourable transition. Diamond being the higher energy structure at standard conditions means that it is metastable, the only reason it doesn't spontaneously convert to graphite is due to a large energy barrier along the reaction coordinate^[3]. Graphite consists of carbon atoms in a hexagonal structure with sp^2 hybridised orbitals. Each atom-layer of graphite, namely graphene, is stacked one on top of another, with each layer interacting weakly via the van der Waal's interaction. These inter-layer bonds are long and weak and are thus easily broken. This manifests in graphite being considerably weaker than diamond, especially along the plane, however, it finds specific use as lubricants and pencils due to graphene layers easily slipping past each other^[4].

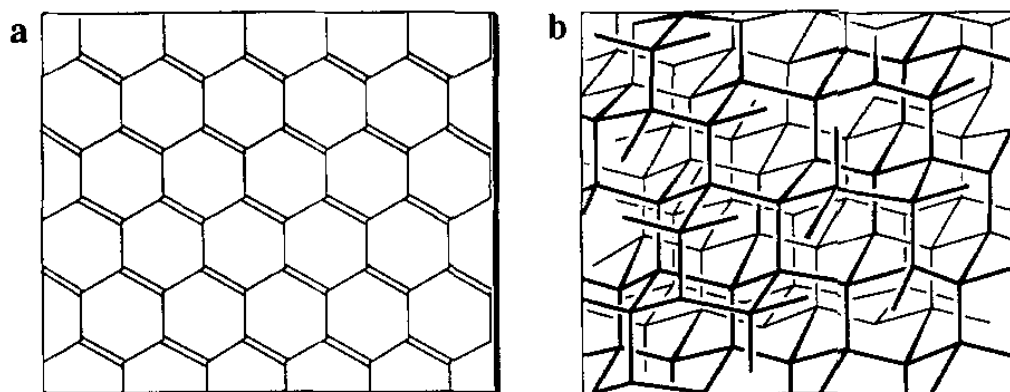


Figure 1: Structure of (a) a plane of graphite (graphene) and (b) diamond^[5].

1.1.2 Electronic Properties

In the case of diamond, each carbon is bonded to four adjacent carbons, satisfying its valency and leaving no mobile electrons. This results in a large band gap of $\sim 5.5 \text{ eV}$ to promote an electron into

the unoccupied conduction band from the occupied valance band^[6]. Diamond is, therefore, quintessentially an electrical insulator. Graphite however, due to its sp^2 hybridised bonding character, can conduct along its planes but not perpendicular. This is due to metallic-like bonding constituting the planes, but long-range van der Waals type bonding in between them. This gives graphite useful electronic applications such as electrochemical electrodes and electric brushes^[4].

1.1.3 Synthesis

Even though diamond has plenty of desirable characteristics and properties that would give it immense industrial capability, only specific applications exist, such as an abrasive or cutting tools, due to diamond's scarcity and the fact that its generally found in nature as a fine particulate. However, scientific breakthroughs over the last 70 years in methods to synthesise diamond have expanded diamonds interest into passive applications^[7] and quantum photonics^[8,9].

The first method of diamond synthesis was in 1955 by the General Electric research laboratory by converting graphite to diamond in metastable conditions using extremely high pressures and temperatures, which was later dubbed the High Pressure, High Temperature (HPHT) synthesis^[10]. However industrial synthesis only really became feasible in the 1990s, when it was possible to grow a diamond of suitable size and purity for use as jewellery^[11].

In 1962, the first documented synthesis of diamond in metastable conditions using Chemical Vapour Deposition (CVD) was achieved by William. G. Eversole^[12]. CVD works by creating a volatile vapour above the substrate, which reacts and deposits onto the surface. The surge in interest of CVD can be attributed to the National Institute for Research in Inorganic Materials (NIRIM), who designed several different CVD techniques, one of which was Microwave Plasma CVD (MWCVD)^[13,14]. Currently, to grow diamond films using the MWCVD method, a ratio of ~100:1 of Hydrogen to Methane is used at temperatures above 800°C to produce a polycrystalline film with a grain size in the nano to micron scale, and thicknesses from nm up to mm, dependant on growth times and specific conditions.

For quality growth to occur hydrogen must be present. The hydrogen radical plays a hugely important role in diamond growth chemistry:

1. Etches sp^2 carbon preferentially over sp^3 , removing it back into the gas phase, clearing any graphitic clusters that may form^[15].
2. Converts inactive CH_4 molecules into reactive CH_3 radicals, which can facilitate growth^[15].

3. Abstracts H off hydrocarbons attached to the diamond surface, which creates an active site for growth^[15].
4. Stabilises the diamond surface by reacting with dangling bonds^[15].

There are two distinct stages of diamond film formation: nucleation and growth. In general, the rate of nucleation on almost any substrate (except a diamond substrate) is extremely low^[16]. Methods of seeding have been developed to increase rate of nucleation, from manually scratching diamond into the substrate^[16], or treating the substrate in an ultrasonic bath with a diamond colloid^[17] to generate active sites for nucleation. Adhesion of a diamond film to a substrate depends both on pre-treatment, and on the capability of the substrate material to form a carbide. Metals like copper do not readily react with carbon, so seeding must be seen a pre-requisite for growth. Molybdenum on the other hand reacts readily with carbon to form a carbide, however in order to get useful rates of growth, they're often seeded anyway^[18].

Changing the composition of the gasses in the plasma can have dramatic effects on the structure of the diamond film produced. Hydrogen is of vast importance in forming high quality diamond films, methane fractions of 5% or greater will lead to diamond films that are increasingly graphitic in content^[19]. It has also been shown that introducing argon into the plasma can facilitate the growth of smooth nanocrystalline diamond films. ~~This discovery has led to the belief that the precursor to diamond growth is actually the C₂ radical, which increases in concentration with increasing Ar^[20,21].~~ This C₂ radical has recently been directly observed in a CH₄/H₂ plasma using optical emission spectroscopy^[22].

The effect of pressure on the rate of growth can be understood by kinetics, with increasing pressure increasing both the rate of species travelling to the surface and the temperature of the substrate. Once the temperature increases to the point where the rate of desorption of active species becomes comparable to the rate of incorporation of these active species, the growth rate starts to decrease^[23].

1.1.4 Doping and Semiconducting Diamond

One of the biggest advantages of CVD over other methods is that impurities can be purposefully introduced into the diamond lattice during growth to give the resulting film semiconductor properties. The two types of doping are n- and p-type. The p-type doping can be achieved by adding boron-containing molecules to the vapour mixture during growth^[24], or by ion implantation^[25]. The n-type doped films can be made by adding phosphorous containing gasses into the plasma during growth, such as PH₃^[26]. Alternatively, nitrogen can be used to make n-type doped diamond by including N₂ gas in the plasma producing a film with up to 0.2% nitrogen content^[27].

The p-type doping in diamond involves substitutionally adding an impurity atom with three valence electrons in place of carbon's four, which creates an electron vacancy. At a concentration of tens to hundreds of parts per million distributed throughout the diamond lattice, these vacancies create an acceptor level slightly above the Valence Band Maximum (VBM). For boron in diamond this acceptor level is ~ 0.36 eV above the VBM^[28]. At room temperature electrons can easily be promoted up to this acceptor energy level, leaving positively charged holes in the valence band, allowing electrical conduction. This shifts the Fermi level towards the valence band. The n-type doping substitutes an atom with one extra valence electron into the lattice. This valence electron produces a donor level below the Conduction Band Minimum (CBM). For nitrogen and phosphorus, this level lies at 1.70 ^[29] and 0.37 eV^[30] below the CBM respectively. The nitrogen doping gives a deeper level than phosphorus, meaning nitrogen-doped diamond does not become conductive until it is heated several hundreds of degrees above room temperature.

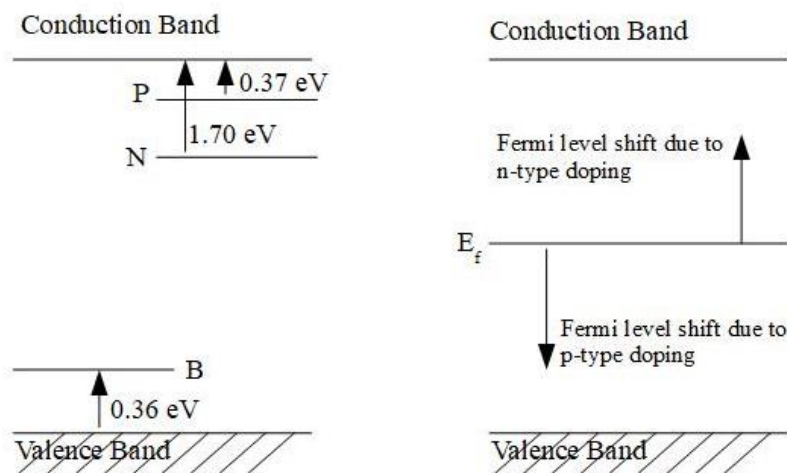


Figure 3: Band structure of doped diamonds, with associated donor levels and transitions (left), and the shift in diamonds Fermi level, E_f , due to the different types of doping (right).

Due to the inhomogeneity of doped diamond, atoms at the surface may not be able to satisfy their valence leading to uncompensated charge which alters the energy of the band at the surface with respect to the bulk. This causes the bands to bend at the interface, upwards in the case of n-type doping, and downwards in the case of p-type.

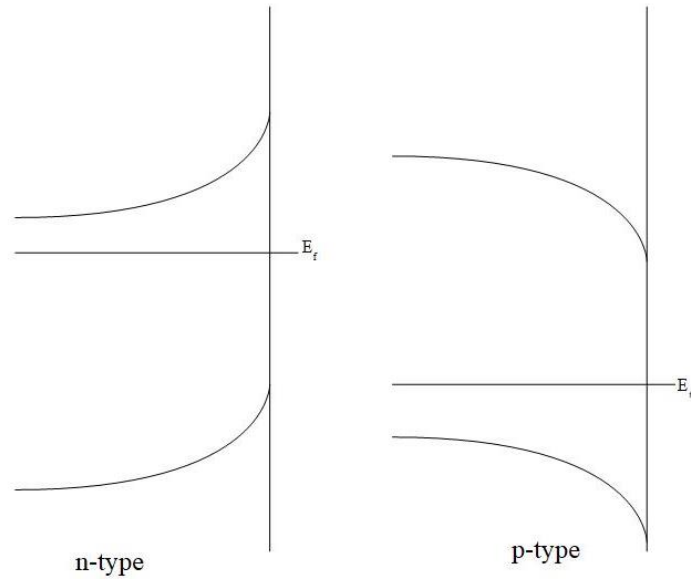


Figure 4: Band structure of p- and n-type doped diamond, illustrating the band bending at the surface, where E_f is the Fermi level.

1.1.5 Hydrogen Termination

In a diamond crystal, once an electron has been promoted to the CBM there remains an energy barrier preventing electron emission, termed the electron affinity, χ . However, by terminating a diamond surface with hydrogen, it develops a useful property, a Negative Electron Affinity (NEA). Electrons in the CBM now no longer face an energy barrier on escaping into vacuum and it's been shown that relative to the non-terminated diamond surface, H-terminated diamond surfaces emit electrons with a yield several orders of magnitude greater^[31]. This opens a lot of interesting avenues for diamond as a low work function material, such as its use as a cold cathode emitter and UV photocathodes^[32,33].

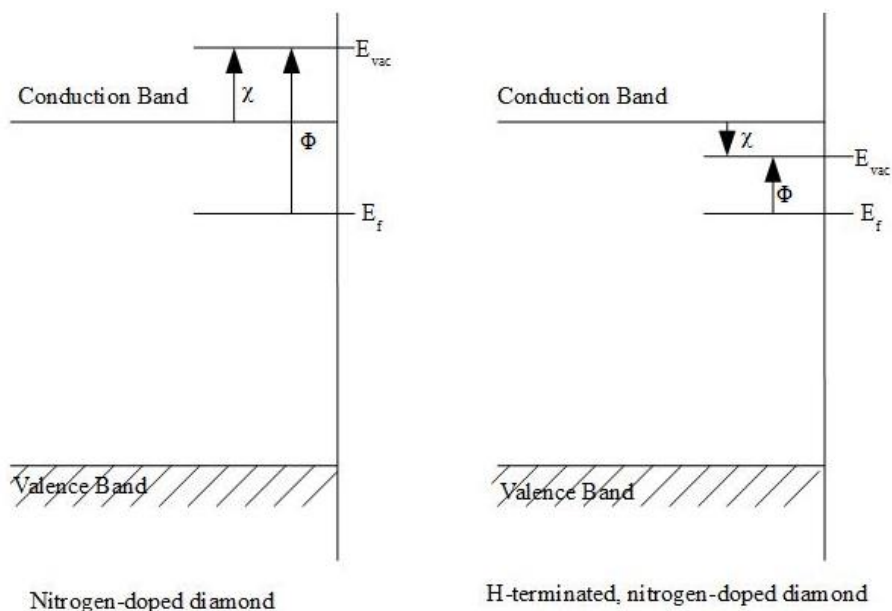


Figure 5: The electron affinity, χ , the work function, Φ , the Fermi-level, E_f , and the surface-vacuum level, E_{vac} , of bare nitrogen-doped diamond (left), and H-terminated, nitrogen-doped diamond (right). The band bending due to doping has been omitted for clarity.

The mechanism for such a phenomenon is thought to be attributed to the dipole of the C-H bond. Electron density is forced closer to the C due to the differing electronegativities, resulting in some electron density slightly filling up the conduction band^[34]. The tunability of the hydrogen-terminated diamond surface has recently been reported and shown in figure 6^[35].

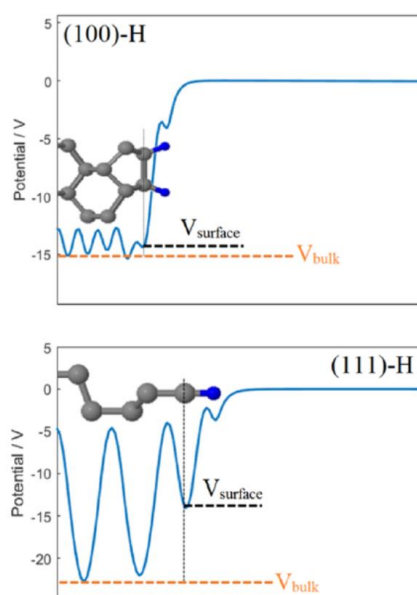


Figure 6: Density functional theory calculations for the electric potentials of the (100) and (111) surfaces of diamond terminated with hydrogen. Carbons atoms in grey, hydrogen atoms in blue^[35].

1.1.6 Surface Morphology

The three low index planes of diamond are (100), (110) and (111), each showing 4-, 2-, and 6-fold degrees of symmetry respectively, have been determined by LEED investigations^[28]. The importance of understanding diamond's surface morphology cannot be understated. The growth of diamond is not fully understood, and technological advancements involving semiconducting diamond require a deeper knowledge of the growth mechanisms for these 3 surfaces.

As explained in the previous section, the dipole present after terminating with hydrogen causes the surface to develop an NEA. However, it is not just the difference in electronegativity that determines the magnitude and sign of the electron affinity, but also the relative symmetry of that charge distribution, determined by the orientation of the surface^[36]. It has been shown however that the 3 low index planes of diamond do show a NEA^[37].

Table 1: Data for electron affinity and work function for 3 different monoterminated diamond surfaces, calculated experimentally by UPS^[37].

Surface	Electron Affinity, χ / eV	Work Function, ϕ / eV
C(100)-(2x1):H	-1.0	3.9
C(110)-(1x1):H	-0.9	4.2
C(111)-(1x1):H	-1.0	3.0

1.1.7 Grain Boundaries

A grain boundary is a 2D defect in a material, which separates two or more crystallites in a polycrystalline material. Understanding grain boundaries for diamond films is of vital importance as it is the origin of CVD diamond's interesting properties^[38]. The size of grain boundaries is essentially controlled by two factors, a) Growth conditions and b) Growth length.

- a) As mentioned in section 1.1.3, hydrogen is hugely important in growing diamond films, owing to its preferential etching of sp^2 carbon. If grown in a slightly hydrogen poor environment, a very graphitic, sp^2 growth can occur, with grain boundaries on the order of a few nanometres. If using the same conditions the film was grown in a hydrogen rich environment, a more diamond-like growth occurred, with larger grain boundaries^[39].
- b) At the start of a growth, post-nucleation, the small nano-scale crystals will be of essentially random orientation. However, as the reaction coordinate progresses, there will eventually be a preferential growth of a certain index orientation, leading to an anisotropy of growth velocities. The results of this can be clearly seen in figure 7, where the sharpened tip orientation grows

slower, such so that its growth gets stunted. There are two results of this, 1) Longer growth times leads to a preferential orientation of crystals, and 2) Longer growths lead to a larger grain boundary^[40].

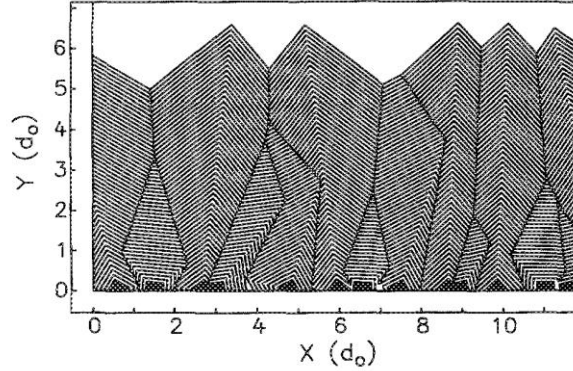


Figure 7: Computer simulation of a column like film, showing the eventual preference in orientation for a long growth film^[40].

1.2 Thermionic Emission

1.2.1 History

The phenomenon was initially reported by F. Guthrie in 1873, when he observed negatively charged bodies would lose their charge when heated, and positive ones did not. He hypothesised an ‘electrical coercitive force’ which diminished with increasing temperature^[41].

1.2.2 Richardson’s Law and the Theory of Thermionic Emission

In 1901, O. W. Richardson released a paper named ‘*On the negative radiation from hot platinum*’, which defined the first quantitative explanation for the thermionic phenomena. He observed that current out of a heated body would decrease in an Arrhenius manner, using a Maxwell-Boltzmann distribution of velocities for electrons. Around 3 decades later, the theory would be refined using a Fermi-Dirac distribution, resulting in equation (1), where j_s is the current density, A is the Richardson constant, T is temperature and Φ is the work function of the material^[42].

$$j_s = A_R T^2 e^{-\frac{\Phi}{kT}} \quad (1)$$

Equation 1: Richardson equation, where j_s is emission current density, A_R is the Richardson constant, T is the temperature, Φ is the work function and k is the Boltzmann’s constant.

The work function of a material is defined as the amount of energy required to expel an electron to vacuum from the Fermi level. In thermionic emission this energy comes specifically from thermal excitation. It is logical to then conclude reducing the work function of a material would, at some temperature, T , increase the thermionic emissivity.

The Richardson equation is mainly illustrative in nature. Even though the Richardson constant can be accurately predicted for metallic like substances, it tends to break down for nanostructured materials, such as carbon nanotubes^[43]. Often A_G is written as $A_0\lambda_R$, where A_0 is a universal constant, and λ_R is a material-specific correction factor^[44].

1.2.3 Beta Enhancement

It's been shown over the past 10 years that electromagnetic radiation can improve the emissivity of thermionic surfaces. In 2010, J. W. Swchede *et al* released a paper on photo-enhanced thermionic emission with GaN samples, which proposed using a photovoltaic cell in conjunction with a thermionic energy converter, greatly increasing the theoretical efficiency of the device to above 50%^[45]. More recent work *circa* 2016, done by *et al* A. Croot at the University of Bristol, presented beta radiation as a method of enhancing thermionic emission of nitrogen-doped, diamond thin films. Figure 8 shows results from that paper, with the beta radiated run, at cycle 20, showing a 2.7-fold enhancement relative to the non-beta^[46].

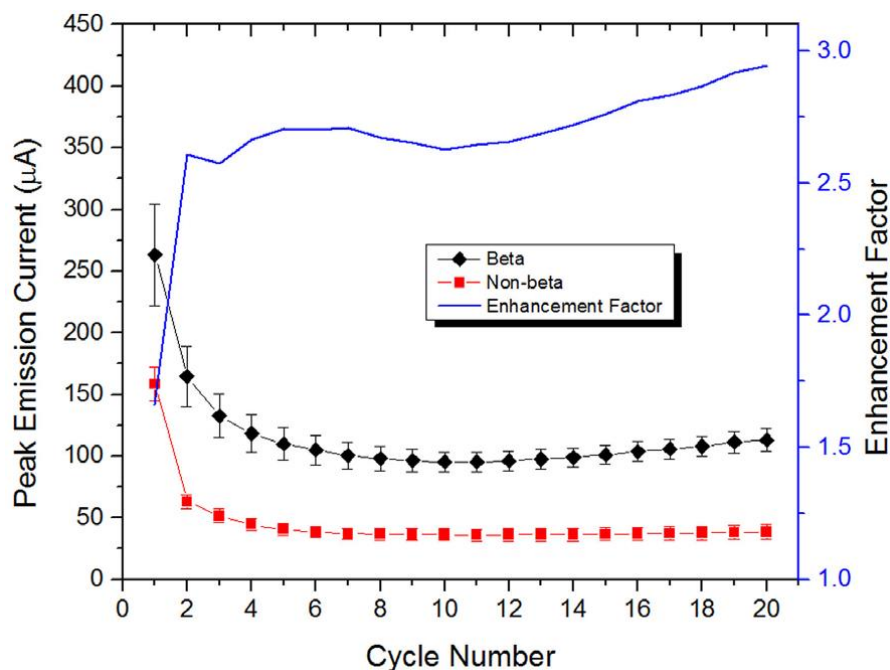


Figure 8: Data presented by A. Croot *et al* showing the enhancement of a diamond thin, nitrogen-doped film when radiated by a beta source. Source was ^{63}Ni (2.6 MBq)^[46].

The paper authored by A. Croot *et al* also undertook an investigation into the mechanism of beta enhanced thermionic emission, where multiple mechanisms were discussed, along with their likelihood. Here is a summary of these potential mechanisms.

1. *Secondary Electron Emission (SEE)*: Beta particles imparting their energy to the electrons, enough for emission to occur. This was deemed to be unlikely to be the dominant effect, as current increase was calculated to be on the order of tens of pA^[46].
2. *Formation of electron hole pairs*: When high-energy beta particles travel through the diamond lattice, they generate electron hole pairs, which would enhance conductivity of the sample increasing surface charge carrier replenishment. A second experiment was set up to measure the conductivity with and without a beta source between 300 – 600 °C. Irradiating with beta yielded no difference in conductivity. This was then further backed up by a calculation which predicted no more than 600 electron hole pairs being active at any one time, and thus deemed unlikely to be having any noticeable effect^[46].
3. *Skewing the Fermi-Dirac distribution*: Beta particles undergo inelastic collisions with electrons in the bulk, skewing the existing valence and conduction band Fermi-Dirac distribution of energy. Upward band bending results in a partial energy barrier to emission, resulting in some conduction band electrons, deemed easy to emit, held in the bulk. The skewing of the conduction band Fermi-Dirac distribution results in a larger proportion of conduction band electrons being able to traverse this barrier^[46]. This hypothesis was related to findings presented by Domenech-Garret *et al* which concurred with this theory^[47]. This was then deemed to be the dominant effect.

1.3 Thermionic Energy Converters and Other Applications

1.3.1 Thermionic Energy Converter Overview

Simply, a Thermionic Energy Converter (TEC) consists of a hot cathode emitting electrons to an anode where the anodes Fermi level is lower than that of the cathode. The cathode and anode are connected in circuit. This allows for the thermally stimulated emission of electrons to generate a current (see figure 9).

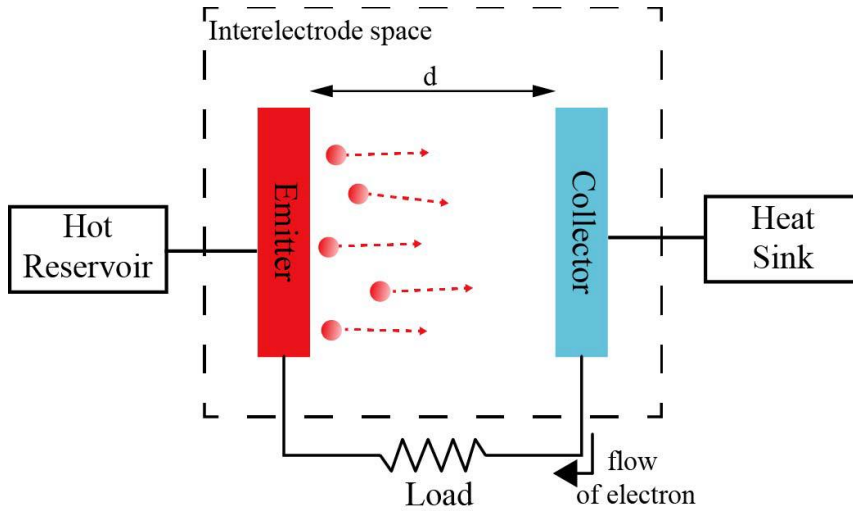


Figure 9: Schematic diagram of a TEC^[48].

The efficiency of the TEC, like any heat engine, is limited by the Carnot cycle (equation 2). It is seen that, using equation 2, the efficiency of a Carnot heat engine may be maximised, by reducing the temperature of the cold sink, T_c , and increasing the temperature of the hot sink, T_h .

$$\eta = 1 - \frac{T_c}{T_h} \quad (2)$$

Equation 2: Efficiency of a Carnot cycle, where T_c is the temperature of the cold sink, T_h is the temperature of the hot sink, and η is the efficiency.

The real advantage of a thermionic energy converter relative to conventional heat engines, is that it contains no moving parts. This means that there are zero mechanical losses, increasing the theoretical efficiency achievable.

1.3.2 Research into Thermionic Energy Converters

The first idea of a thermionic energy converter came from Schlichter in 1915^[49]. Then later in the 1950's, where G. N. Hatsopoulos *et al* designed 2 different types of TEC's whilst working on thermoelectric engines, namely vacuum TEC's, and vapour TEC's^[50]. In general, vacuum TEC's (figure 9a) has a small, highly evacuated chamber hosting the 2 electrodes. These electrodes needed to be very close (microns), to lessen the amount electrons traversing the vacuum at any one time, to reduce the negative effect on efficiency due to the space charge effect^[51]. However, at such small gap distances between the electrodes, there tends to be a thermal leakage from the hot to the cold sink, reducing the Carnot efficiency. There has recently been a resurgence in research on vacuum TECs due to hydrogen-terminated diamond's NEA theoretically being able to mitigate the space charge effect^[52,53].

The most widely researched system, the vapour TEC (figure 9b), unlike the vacuum system, did not suffer from the negative effects of a build of space charge in the interelectrode space due to

employing a positively charged vapour to neutralise it, often caesium due to its low ionisation energy^[54]. These energy converters were predicted to have theoretical efficiencies of over 30% but limited by the 90% Carnot cycle limit^[55].

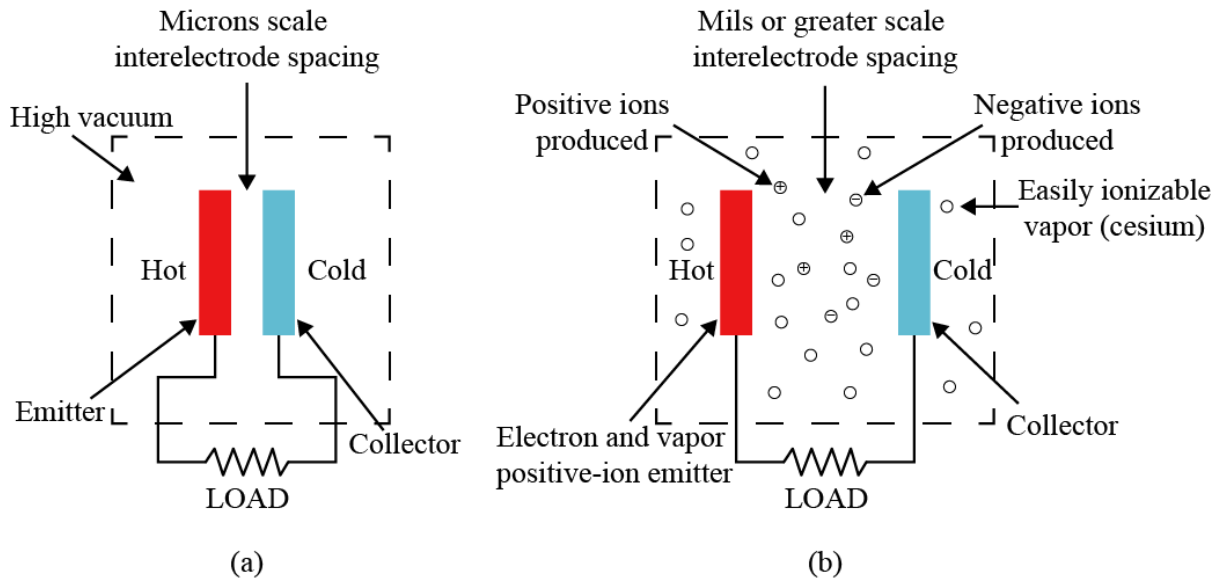


Figure 10: a) Schematic of a vacuum TEC, and b) Schematic of a vapour TEC^[48].

1.3.3 Diamond Emitters

Research into TEC's stagnated for a long while due to low-cost, chemically stable, low work function material being very difficult to isolate. Along with diamond, other materials have been proposed for emitters, such as barium oxide, BaO, deposited on polycrystalline silicon with a layer of tungsten in between which showed a low work function of 1.2 eV, and thermal stability above 1000 °C^[56].

For a material to be a good emitter, it must have 3 characteristics, a) low work function, b) low electrical resistivity, and c) thermally stable at elevated temperatures of greater than 700°C. Addressing (a), when nanocrystalline films are nitrogen-doped and H-terminated, the surface develops a negative electron affinity and subsequently a low work function, as previously discussed. Addressing (b), even though diamond crystals are extremely resistive ($\sim 10^{16} \Omega\text{m}^{[57]}$), nanocrystalline diamond has a large density of grain boundaries, sp^2 hybridised carbon, which makes it markedly more conductive (in the range of $10 - 10^6 \Omega\text{m}^{[57]}$, dependant on dopant, dopant concentration and grain boundary density). The main issue with nanocrystalline diamond for emitters is point (c). Hydrogen has been shown to desorb from cathodes at elevated temperatures above 700 °C^[58], which would lessen the NEA, subsequently diminishing the work function. Interesting observations were made by Koeck *et al* however, when the emitter in the device was contained in a dilute ambient hydrogen atmosphere, the NEA did not reduce,

and the device showed stable operation at 750 °C. This was by virtue of the surface of the emitter and the hydrogen atmosphere equilibrating^[59].

1.3.4 Other Applications of Diamond Emitters

Field Emission Display (FED): Flat panel displays are widely used in many different applications, but often have poor brightness and viewing angle. FED's hoped to iron out these issues. They work by having a matrix of micro-cathodes with a small vacuum gap to a panel of phosphor pixels. A voltage is applied across the cathode and panel, such that the micro-cathodes emit electrons and excite the pixels. Polycrystalline, nitrogen-doped, H-terminated diamond films have been proposed as a material for these micro-cathodes^[60].

Photo-catalytic reduction of N₂: Reduction of N₂ to NH₃ is often hindered by poor binding to the catalysts surface. Illuminated H-terminated diamond works round this problem by producing facile yields of electrons in solution which reduces N₂ at ambient temperatures and pressures^[61].

Electron beam lithography: Heavily phosphorus doped diamond shaped to small sharp protrusions on the surface turn it into a single point emitter. Because of doped diamonds low work function, it can produce electron beams of high current density and low energy distribution. This, relative to other electron beams, would have an improved writing speed^[62].

1.4 Review of Work Done by the University of Bristol

This section briefly outlines work by the University of Bristol's diamond lab which is pertinent to this report. The work outlined in this report aims to carry on the research in specific areas.

1.4.1 Growing Nitrogen-Doped Diamond

Two reports presenting very detailed research on the growth of nitrogen doped films, done by B. S. Truscott *et al* and published in 2015 and 2016, essentially lay the foundation for the work done here by being able to reliably grow nitrogen-doped films using MWCVD. Optical emission spectroscopy was used to probe the energy distribution in the radical species within the plasma, and in conjunction with 2-D coupled kinetic and transport modelling, a very detailed understanding of C, H and N's chemical reactivity in the plasma were afforded^[63,64].

1.4.2 Field Emission from Grain Boundaries

V. Chatterjee *et al* released a publication in 2014, where direct field emission (emission stimulated by the presence of an electric field) of electrons was directly observed using atomic force microscopy, for H-terminated, polycrystalline diamond. The findings confirmed that the majority of emission does in fact occur at the grain boundary^[65].

1.4.3 Variation of Work Function Across the Surface of H-terminated Diamond

In work by J. H. Lay in 2011, kelvin force microscopy was used to measure the contact potential, and by extension, the work function, of different areas on 2 boron-doped diamond films. Observations consisted of the contact potential varying across the surface up to 350 mV, which was dependant on topographical features, localised dopant concentrations, and the presence of sp² hybridised carbon. When making devices involving surface electronic properties, these factors must be considered^[66].

1.5 *Project Overview*

In this project the thermionic emission properties of H-terminated, nitrogen-doped diamond films of different thicknesses and grown on diamond and molybdenum will be tested, to further elucidate the thermal properties of these films.

2 Methodology

2.1 *Sample Growths and Preparations*

2.1.1 Apparatus

All samples were grown using MWCVD, in a 2.45 GHz, 1.5 kW ASTeX-type reactor. Growth occurred in a hydrogen, methane and nitrogen plasma (4.2% methane in hydrogen, 2.4% nitrogen in methane), with forward power varying from 1200-1400 W, pressures from 120-140 torr, and temperatures from 800-900 °C. During growth the reflected was tuned to 0-1 using the tuning antenna. The growth lengths were altered to vary the thickness of the films.

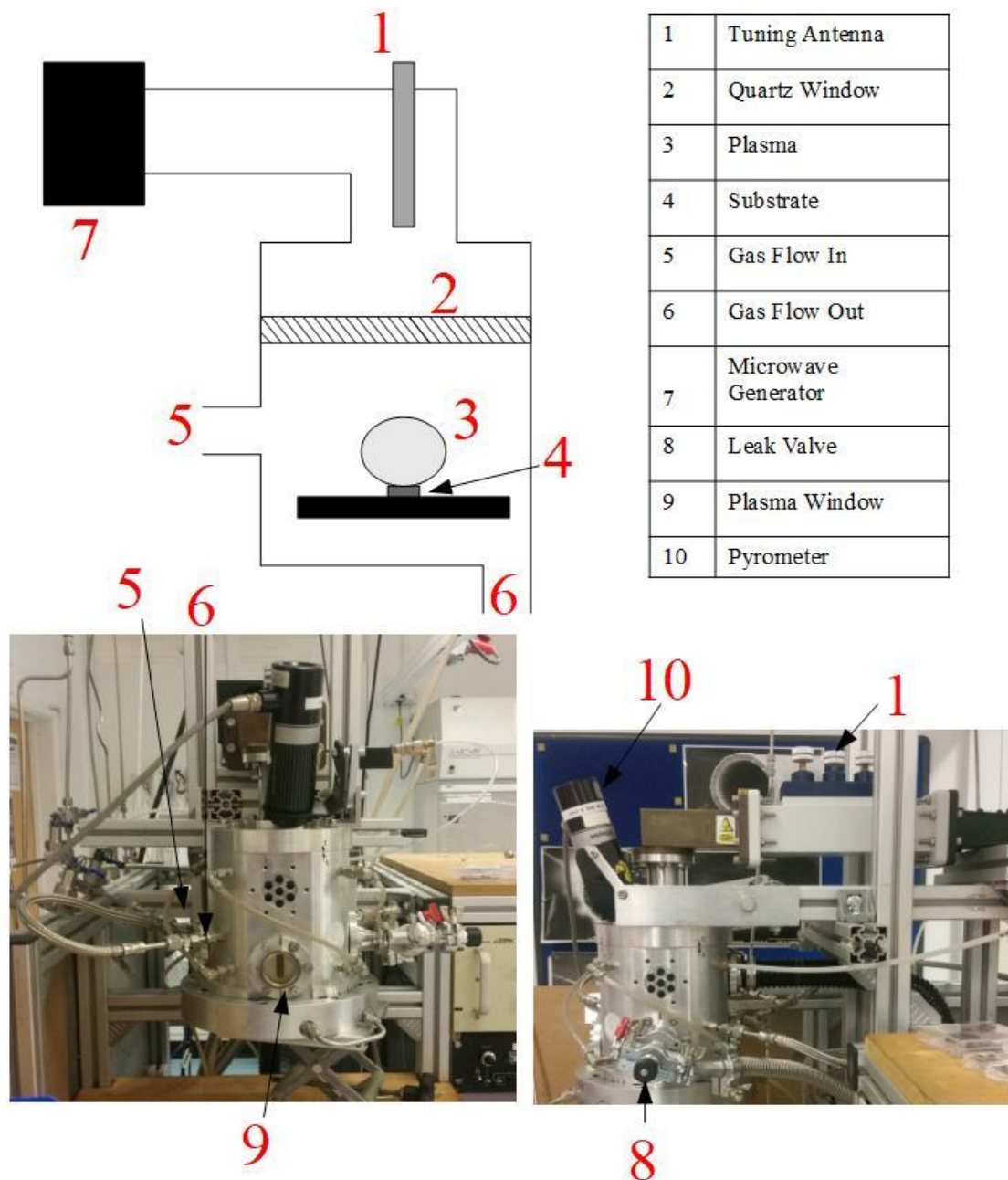


Figure 10: Top left) Simple pictorial view of the MWCVD reactor, Bottom left) Front on view of MWCVD reactor, Bottom right) Side on view of MWCVD reactor.

2.1.1 Diamond Backside Growth (Samples D1 and D2)

Before the diamond film was grown onto the thermal grade diamond substrates, the backside was coated with a film of poor-quality diamond to improve radiative heating. This was done, by MWCVD, by using a 11% CH_4 in H_2 plasma, resulting a considerably graphitic growth which was black in colour.

Table 2: Conditions for both backside poor-quality diamond growth for samples D1 and D2.

<u>Run Time (min)</u>	<u>H₂ Flow Rate (sccm)</u>	<u>CH₄ Flow Rate (sccm)</u>	<u>N₂ Flow Rate (sccm)</u>	<u>Power (W)</u>	<u>Pressure (Torr)</u>	<u>Temperature (°C)</u>
90	266	30	3	1300	140	1130

2.1.2 Diamond Substrate Growths

A total of two films, of varying thicknesses, were grown on diamond. This consisted of a short length growth, D1, and a longer growth time, D2. The substrates used were 10 mm × 10 mm thermal grade diamond. Shown in table 3 are the specific conditions used for each growth.

Table 3: Specific conditions for the growths of the diamond films grown on thermal grade diamond. Note that the temperature given is roughly an average and would have varied slightly (10 – 20 °C) over the course of the growth.

<u>Sample</u>	<u>Run Time (min)</u>	<u>Pressure (Torr)</u>	<u>Power (W)</u>	<u>Temperature (°C)</u>
D1	12	140	1400	901
D2	360	140	1400	910

2.1.3 Molybdenum Substrate Growths

Two film thicknesses were attempted on molybdenum, however only one was successful. This consisted of a short growth, Mo1, and an unsuccessful attempt at a longer growth period. The substrates were 10 mm × 10 mm molybdenum.

Table 4: Specific conditions for the growths of diamond films on molybdenum substrates. Again, note the temperature will vary by the same degree during the complete growth time.

<u>Sample</u>	<u>Run Time (min)</u>	<u>Pressure (Torr)</u>	<u>Power (W)</u>	<u>Temperature (°C)</u>
Mo1	12	120	1200	890

Before growth, the molybdenum substrates were seeded with de Beers nano scale diamond powder by manually abrading into the surface, then washing with ethanol. This leaves small bits of diamond powder embedded in scratches on the molybdenum surface which become active sites for nucleation during growth.

Any attempts at a longer growth (90 min, 120 min and 360 min) were all unsuccessful due the film delaminating from the substrate. This is due to the thermal expansion coefficient of molybdenum

being greater than that of diamond ($5.4 \times 10^{-6} \text{ K}^{-1}$ for Mo compared to $1 \times 10^{-6} \text{ K}^{-1}$ for diamond)^{[67],[68]}, causing the molybdenum substrate to expand more than the diamond when heated, thus contracting more when cooling. This puts strain on the diamond surface ultimately causing it to break off.

2.1.4 Plasmonic Grating (Sample Mo1)

Molybdenum is a refractory material; it has high chemical and thermal stability at high temperatures however has lacking optical properties, specifically it struggles in absorbing light. To mitigate this, a plasmonic grating on the backside (molybdenum side) of the sample was applied. This grating had a width of $10.6 \mu\text{m}$ per line, the same as the wavelength of light being used, which helped the sample absorb $10.6 \mu\text{m}$ infrared photons^[69]. This grating was applied using an Oxford Lasers Alpha III micromachining tool.

2.1.5 H-Termination

Before every thermionics run, all samples were hydrogen terminated, in the same reactor as used for growth. The terminations needed to be repeated after each experimental run due to the termination not being thermally stable at the highest temperatures used with the thermionics rig. All growths were done in a purely hydrogen plasma, with H_2 flow rate of 300 sccm. The specific conditions for these are shown in table 5.

Table 5: Specific conditions for H-termination.

Sample	Run Segment (min)	Pressure (Torr)	Power (W)	Temperature (°C)
D1	2	90	1200	~900
	2	45	700	~500
	2	45	-	-
D2	2	90	1200	~900
	2	45	700	~500
	2	45	-	-
Mo1	2	90	1200	~900
	2	45	700	~500
	2	45	-	-

Referring to Table 5, the experimental runs presented are segmented into three distinct sections. The first segment involves high power and high pressure, where $900 \text{ }^\circ\text{C}$ was the target. This acts to burn off any unwanted species which are currently terminated to the surface, conditioning it. The second segment involves a decrease in power and pressure, to meet the conditions which allow hydrogen to terminate onto the surface without desorbing; this happens at temperatures below $\sim 600^\circ\text{C}$, where $500 \text{ }^\circ\text{C}$ was the target. In the final segment, the plasma is switched off, whilst keeping hydrogen flow. This

allows the diamond film to cool in a hydrogen atmosphere, which reduces the rate of hydrogen desorption.

2.2 *Sample Characterisation*

The techniques used to analyse the films grown were a combination of Scanning Electron Microscopy (SEM) and Raman spectroscopy.

2.2.1 SEM

All SEM images were taken using a Tescan Vega 3XM scanning electron microscope. Linked to this was the Tescan AT-LAS software package which was used to operate the SEM. Whilst in use, care was taken to not charge the sample, but this proved difficult.

2.2.2 Raman Spectroscopy

All Raman spectra were taken with a Renishaw 1000 Laser Raman Spectrometer, with a 785 nm diode laser. For each sample, 3 different spectra were taken at different locations on the sample in order to increase the data set size, improving accuracy.

2.3 *Thermionic Studies*

For each sample, a total of 4 runs were done, two with a beta source, and two without. The equipment used was a new set up, designed by researchers at the University of Bristol ^[70]. A summary of the equipment described in the next section.

2.3.1 Apparatus

Shown in figure 11 are diagrams detailing the thermionics rig used in this project. The laser (shown in (a)) is a 10.6 μm continuous CO₂ laser (Firestar V40 Series, Synrad), with a maximum power output of 40 W. The laser is guided to the sample with gold coated copper mirrors, and through a ZnSe screen (WG71050-G, Thorlabs Inc.). The emitter-collector assembly is also shown in figure 11 (shown in (b) and in more detail in (c)). The emitter (or sample) is held in place on a quartz plate, which acts as a layer of electrical and thermal decoupling, with molybdenum clamps, which have a secondary function as an electrical connection. The quartz plate sits in a metal cylinder, which in turn sits in a

second quartz plate, which acts as a second layer of electrical and thermal decoupling. The collector is connected to a linear motor shaft, which controls the height of the collector above the sample.

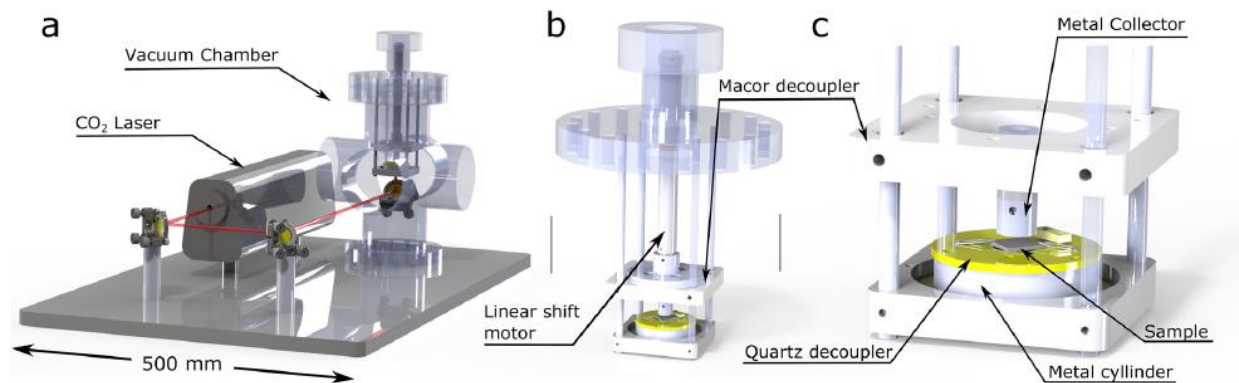


Figure 11: Diagram of the thermionics rig used in this experiment. a) A zoomed out view of the whole apparatus, b) A zoom in of the apparatus centred on the sample holder which inserts into the vacuum chamber, and c) A zoom in of the sample holder specifically showing where the sample is held, as well as the collector^[70].

The temperature is measured by a two-colour optical pyrometer (Spotmeter R160, Land Instruments International Ltd.). The LabView virtual instrument integrates all components of the system and uses a Proportional-Integral-Derivative (PID) closed loop controller to vary the temperature of the emitter, by varying the power output of the laser (figure 12a). Between the emitter and collector there was the 25 V bias applied using a DC power supply (Mastech Linear DC Power Supply – HY3003D, Mastech), over a 200 μm gap distance, and the current is measured with an ammeter (Keithley 2750 Multimeter system, Tektronix) (figure 12b).

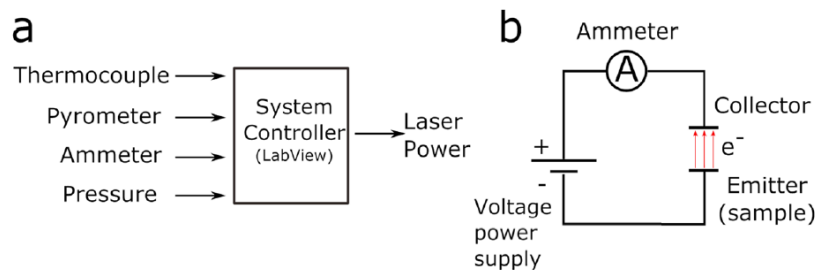


Figure 12: (a) LabView, the virtual instrument which controls laser power and data collection, and (b) Closed current loop containing the voltage power supply and the collector-emitter, with an ammeter ^[70].

2.3.2 Thermionic Runs

For each sample, only four runs were done, two with a beta source and two without. Figure 13 shows the general set temperature ramp, which was pre-set in the LabView software. The beginning of each ramp was the same, shown in table 6. The set temperature ramps changed slightly from sample to sample after reaching 750 °C, with some being stopped earlier due to the current already dropping to negligible levels, and some being left at 750 °C for longer as the current didn't drop as much as expected. For each run, there was a 25 V bias applied between the collector and emitter, with a gap distance of 200 μm , at pressures of $\sim 1.5 \times 10^{-6}$ - 6×10^{-7} torr.

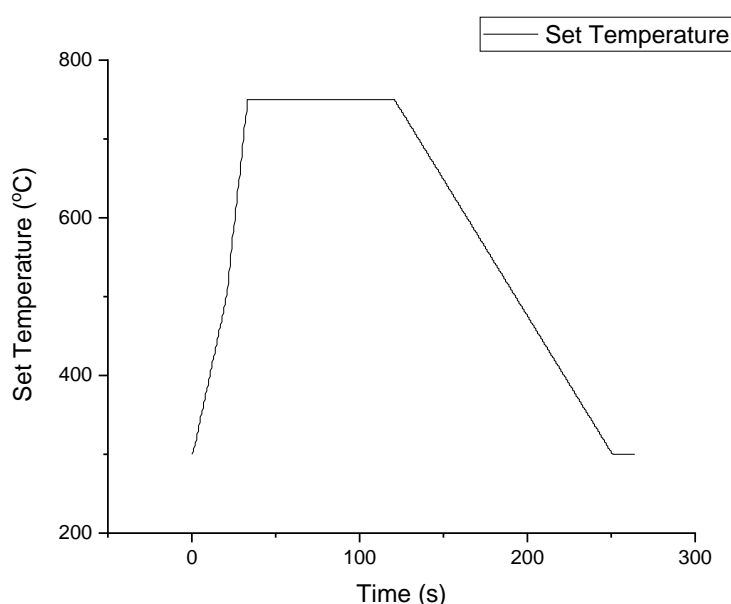


Figure 13: Standard set temperature ramp for each experimental run.

Table 6: The temperatures pre-selected for the ramp.

Time (s)	Set Temperature (°C)
0	300
20.0	550
32.5	750

2.3.3 Beta Enhancement

Two of the four runs for each sample were done with an enclosed beta source. The source located above the sample in a holder attached to the collector, which is shown in figure 14. The beta source was a ^{63}Ni (28 MBq) with 7 mm \times 7 mm dimensions, with the sample having a maximum beta exposure of 74%. ^{63}Ni 's radionuclide characteristics are shown in table 7. Doing a simple calculation

it can be shown that with the set up used, there will be around 20.72×10^6 incident beta particles hitting the sample per second, with an average energy of 17 keV.

Table 7: The radionucleotide characteristics of ^{63}Ni .

β Radiopurity (%)	99<
β E_{average} (keV)	67
β E_{max} (keV)	17

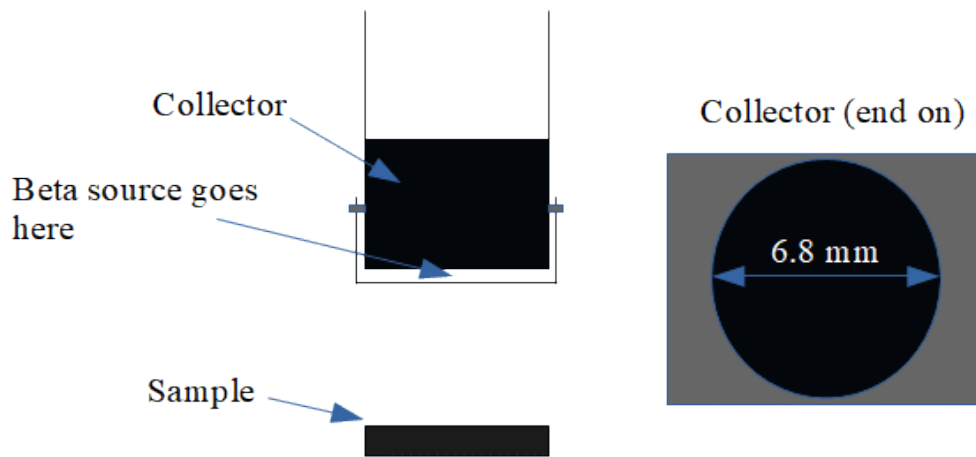


Figure 14: Simple diagram of the collector, with frame to hold the beta source (left). End on view of the frame which holds the beta source, attached to the collector (right). For clarity, the wiring, both quartz decouplers, the metal cylinder and the molybdenum clamps have been omitted.

3 Results and Discussion

3.1 Characterisation

Both Raman spectroscopy and SEM were used to fully characterise the films grown, as well as to make an investigation into the morphology of the different surfaces.

3.1.1 Raman Spectroscopy

Raman was used to identify whether the diamond growth was successful. This can easily be accomplished, as diamond shows a strong characteristic phonon peak at 1332 cm^{-1} in a Raman spectrum^[71], which can clearly be seen for all spectra for all samples, shown in figure 15. Also shown

in figure 15, for the spectra's of D2 and especially Mo1, are broad peaks in region of $1400 - 1600 \text{ cm}^{-1}$ which is indicative of sp^2 hybridised, graphitic-like carbon^[72].

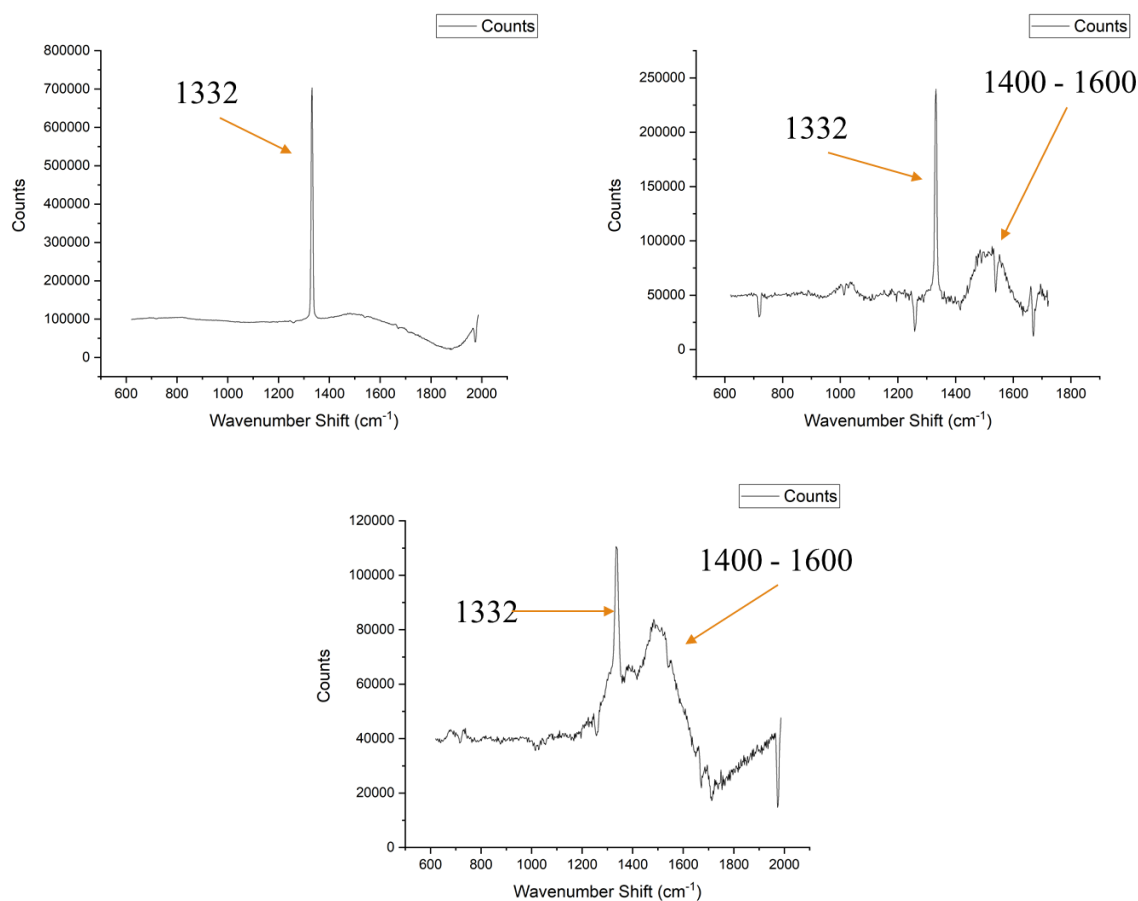


Figure 15: Raman spectra for each sample, D1 (top left), D2 (top right), Mo1 (bottom

3.1.2 SEM Data

SEM was used to investigate the morphology of each sample. Certain micrographs came out slightly blurry (especially for D1 and Mo1) due to the samples charging when scanning, this effect stems from the poor room temperature conductivity the nitrogen-doped films exhibit. To reduce this effect, measures were taken to not charge certain sections for too long and a lower accelerating voltage was selected, however, the effect was impossible to eradicate in its entirety, as there was a minimum time requirement needed in order to take each snapshot.

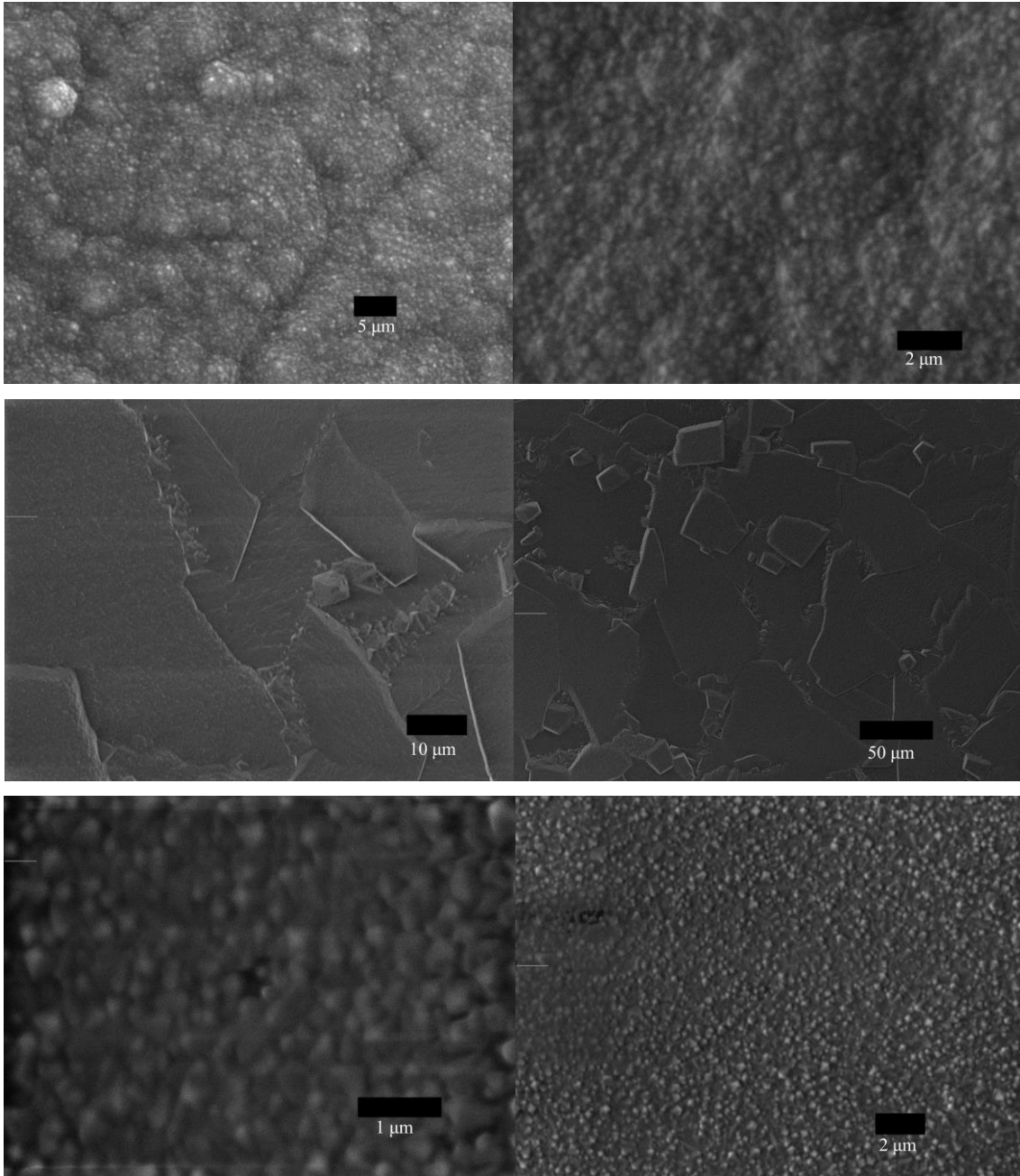


Figure 16: SEM images of D1 (top), D2 (middle) and Mo1 (bottom).

Referring to figure 16, it can be seen that both D1 and Mo1 both have a rough, multifaceted, nanocrystalline surface with no distinct orientation preference. However, D1's crystallites have coalesced, making a rougher surface with distinct topographical features. Mo1 has visibly distinct crystallite domains, indicative of the growth still in the first nucleation phase. Reasoning for the disparity in the 2 surfaces comes from the fact that D1 was grown onto a diamond substrate, with a high density of nucleation sites where growth could occur. The seeding method used for Mo1 would not have facilitated as many nucleation sites, and thus the growth would have occurred much more slowly.

D2 has grown for considerably longer relative to the other two, and has shown a definite orientation preference, with a smoother, microcrystalline surface with a grain boundary size on the order of tens of μm .

3.2 Thermionics Data

3.2.1 Results

In figure 17, the trend of temperature and current against time is shown for a representative data set. At a temperature greater than $450\text{ }^\circ\text{C}$ the current starts to increase, reaching a maximum when the temperature reaches $750\text{ }^\circ\text{C}$, before decreasing. A sharper decrease occurs once the temperature starts to fall, after approximately 125 s . The marked decrease once the maximum temperature has been reached stems from some proportion of the hydrogen termination not being thermally stable at elevated temperatures above $600\text{ }^\circ\text{C}$, which in turn increases the work function of the surface.

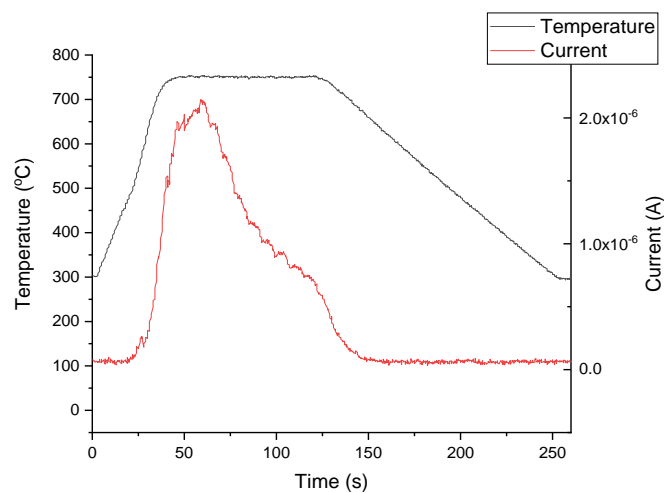


Figure 17: Plot of temperature (left y axis) and current (right y axis) against time. Specific data was taken from no-beta – 1, shown in Table 8.

Table 8 shows data peak current and threshold temperature for all 4 runs attempted. The threshold temperature was defined as the temperature once the current exceeded $0.1\ \mu\text{A}$ (this is the definition throughout the paper). Figure 18 shows a plot of each run superimposed onto the same graph.

Table 8: Peak current and threshold temperature for each run for D1.

Run	Peak Current (μA)	Threshold Temperature ($^{\circ}\text{C}$)
No beta – 1	2.15	460
No beta – 2	4.96	456
Beta – 1	1.43	564
Beta - 2	1.51	469

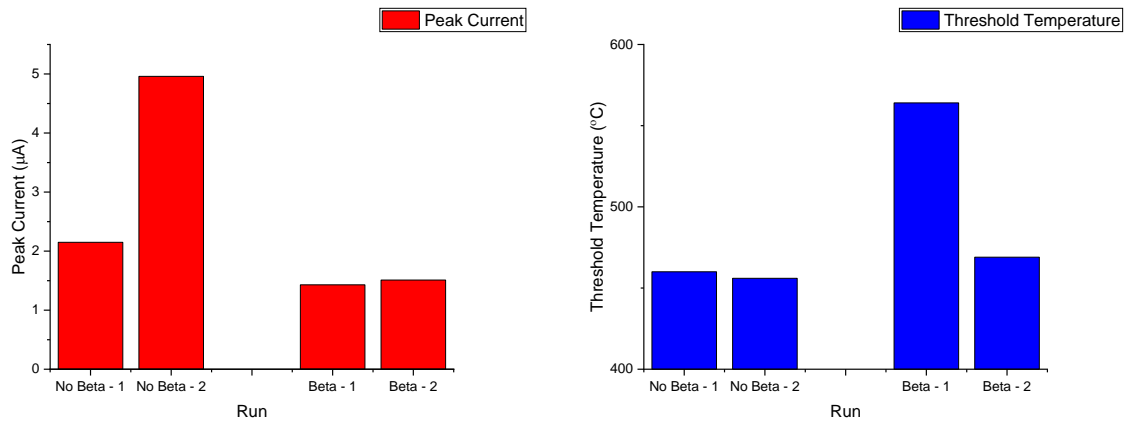


Figure 18: Data from Table 8 presented in a more illustrative manor, as bar charts. Peak current for each run (left) and threshold temperature (right).

For D1, the trend observed in the peak currents for beta and non-beta enhanced runs does not agree with the expected result or the theory. What was anticipated for this was an increase when the sample was radiated with beta but what was observed was a 1.42 – 3.47 – fold decrease in emission current.

Unlike the representative plot in figure 19, which shows the anticipated thermionic behaviour of the sample, the green and red curves slowly increase up to a maximum, before sharply dropping with decreasing temperature. In hindsight these two data sets should have been left at 750 $^{\circ}\text{C}$ until a maximum had been reached.

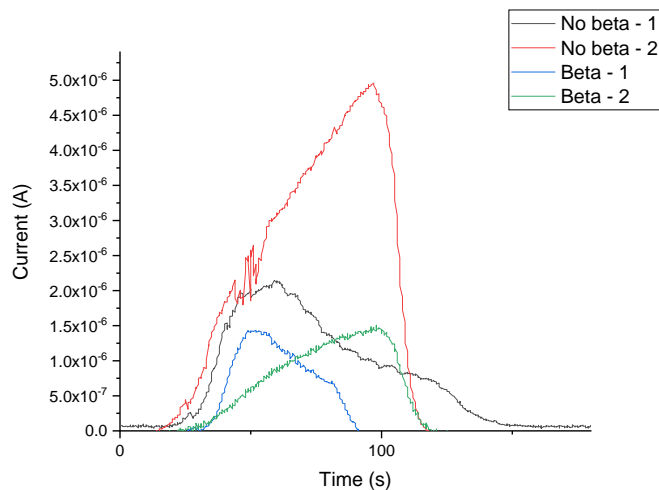


Figure 19: Each run for D1 plotted on the same current against time graph, for comparison.

Figure 20 shows a representative data set for D2. Again, at some temperature the current sharply increases, however once reaching a maximum the slope stays approx. constant, until decreasing with decreasing temperature. The specific trend shown was not at all anticipated and indicates that the work function stayed constant at 750 °C, which is indicative no H desorption from the surface. My belief is that, due to the considerably smoother surface, the H-termination may not have been as stable as previously thought, and that the H desorbed at a considerably lower temperature, or possibly before the run has even been conducted.

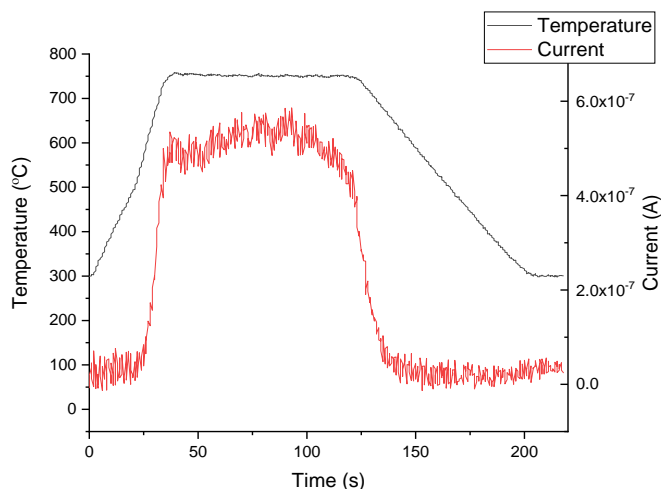


Figure 20: Plot of temperature (left y axis) and current (right y axis) against time. Specific data was taken from no beta – 1 data set.

Table 9 shows all the data from the 3 runs done with D2, the data of which is then plotted in bar charts in figure 18. The second run without beta is missing which was due to an error whilst doing

that run and was planned to be re-done but with time constraints this was not possible. With only 3 data points it's difficult to take any meaningful deductions for the data. What was seen is a 1.07 – 3.41-fold increase in the peak current when the sample is radiated with beta. The data for threshold temperature doesn't seem to follow any trend.

Table 9: Peak current and threshold temperature for D2.

Run	Peak Current (μA)	Threshold Temperature ($^{\circ}\text{C}$)
No beta – 1	0.59	605
No beta – 2	-	-
Beta – 1	0.62	661
Beta - 2	2.01	549

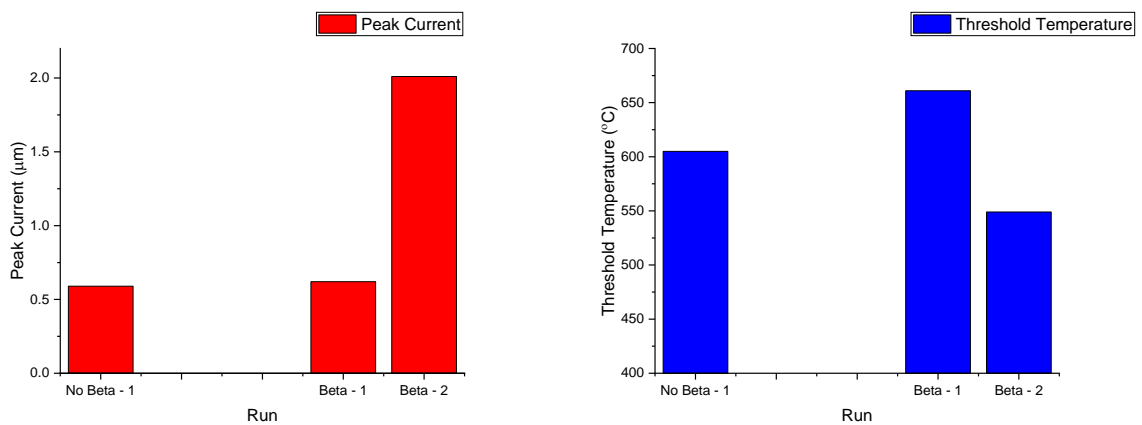


Figure 21: Bar charts illustrating the data from Table 9 for D2.

Unlike the representative curve, the plot for beta – 1 was markedly different than the other 2, with a steady increase up to a maximum, before dramatically dropping off with the decrease in temperature. In hindsight, this run should have been left for longer at 750 $^{\circ}\text{C}$ until a plateau had been reached.

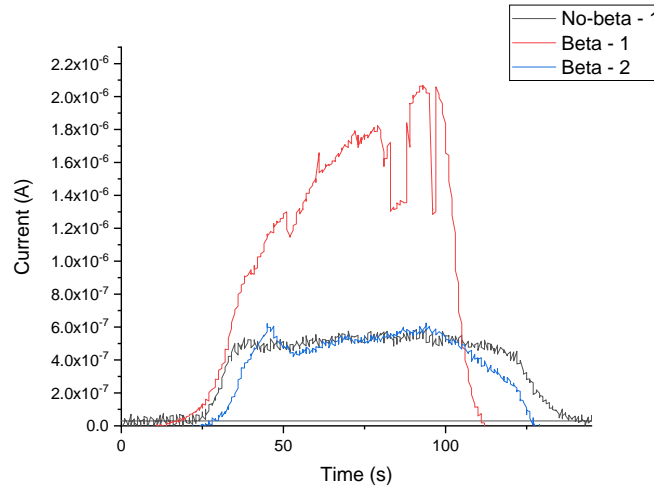


Figure 22: Current against time graphs for all runs done with D2. It must be noted that the sharp drops in current in beta – 1 was due to the laser power suddenly fluctuating.

Figure 23 shows a representative curve for Mo1. The trend is very similar to that of D1; however, a much larger peak current is reached, and subsequently has a much sharper drop off. This curve shown in figure 20 was the one data set in Mo1 that showed the expected outcome but is not indicative of the rest of the data.

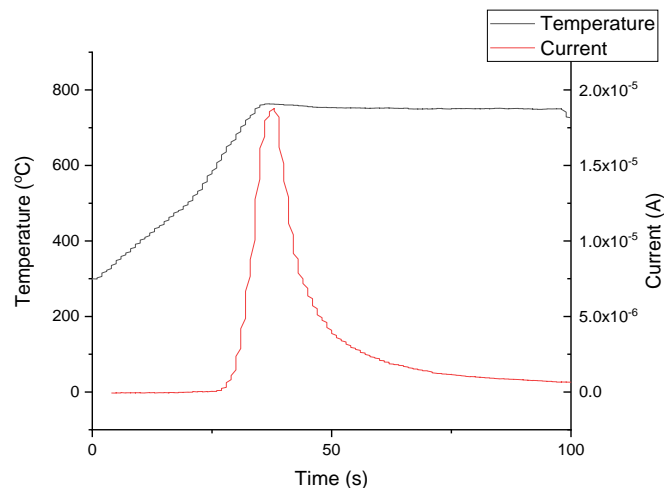


Figure 23: Representative curve for Mo1, showing a sharp increase in emission current, subsequently followed by a sharp decrease, which shallows off.

In table 10 and illustrated in bar charts in figure 24 is the data of peak current and threshold temperature for the runs with Mo1. The trend in peak currents showed a 1.74 – 6.24 – fold increase when the sample was irradiated with beta relative to the non-beta radiated source. There is again no deducible trend in the threshold temperatures, however, as discussed later, this was due to apparatus errors.

Table 10: Data from the runs with Mo1.

Run	Peak Current (μA)	Threshold Temperature ($^{\circ}\text{C}$)
No beta - 1	18.9	524
No beta - 2	18.9	651
Beta - 1	32.8	582
Beta - 2	118	509

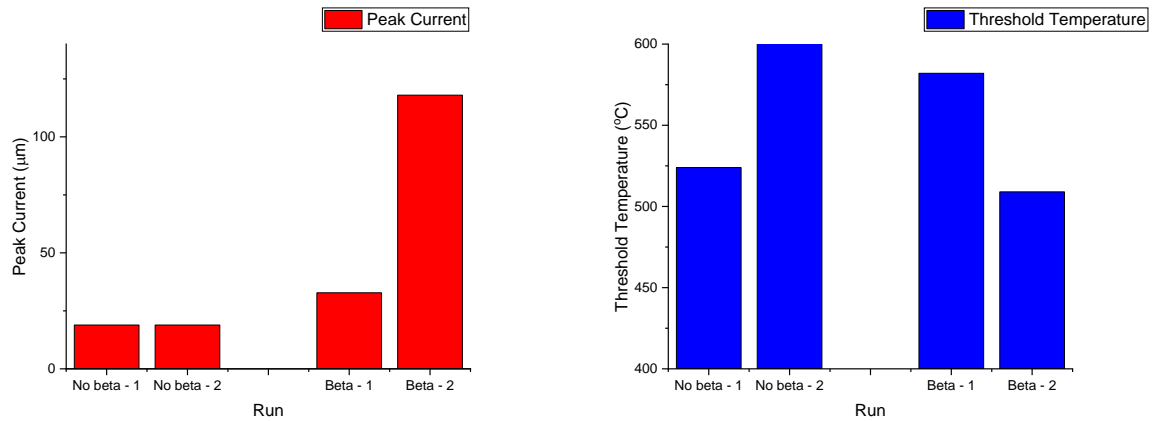


Figure 24: Data plotted in bar charts from table 10.

Again, for this data set, the plots for each run were different. However, unlike the other two samples, they followed the same general trend, a sharp maximum just after the threshold temperature, followed by either a sharp or steady decrease.

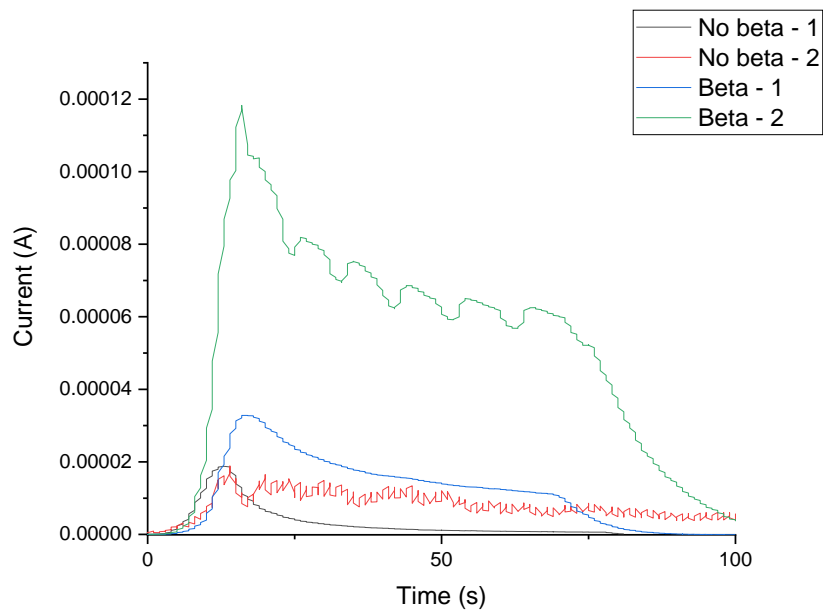


Figure 24: All sets of data taken from the runs for Mo1.

One large issue had with the diamond grown on molybdenum substrate was that for some unknown reason, for three of the four total runs, the actual pyrometer temperature had issues tracking the set temperature. For the no beta – 2 run (figure 24), the laser output was constantly fluctuating by a vast margin, so that the temperature the pyrometer registered was jumping, at the beginning of the run about 250 °C in 2 seconds, however this levelled out slightly to around 100 °C jumps. For the beta – 1 run (top right), the only issue was at the start, before the threshold temperature was reached. Laser power fluctuated so that the temperature saw a maximum fluctuation of ~ 50 °C. The beta – 2 run has the same issue as the beta – 1 run, as well. Once the set temperature ramp had reached 750 °C, the pyrometer temperature registered was incrementally fluctuating above and below 750 °C. This small fluctuation in the temperature had a large effect in the current, due to the current density being proportional to the square of temperature. The source of this difficult to identify, as during the measurement run, direct view of the vacuum chamber wasn't possible. As there were no issues with temperature ramping for all the diamond samples, the issue should originate from the molybdenum substrate, possibly slight reflection of the laser, or slight misalignment of the grating.

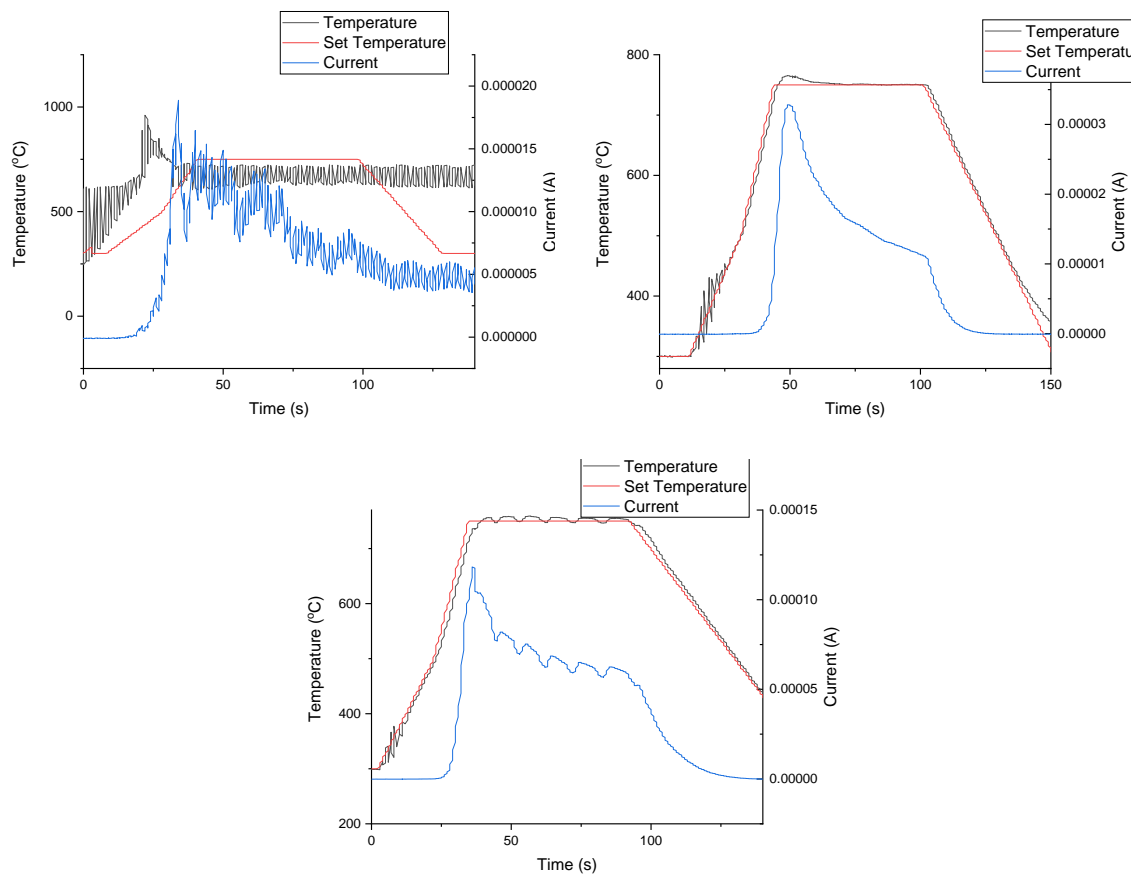


Figure 25: Data sets plotting temperature and current against time for runs no – beta 2 (top left), beta – 1 (top right) and beta – 2 (bottom), to illustrate issues with the laser output.

3.2.2 Effect of Growth Length on Thermionic Emission

In general, D1 showed higher emission currents than D2, except for beta – 2. However, drawing any conclusion based on this comparison is difficult to make with such a small data set of measurement runs. Firstly, when D1 was irradiated with beta, it showed a decrease relative to the non-beta data set, which disagrees with the enhancement theory. Secondly, the missing data point of no – beta for D2 makes it difficult to see any potential outliers. These issues make meaningful comparison of the data sets difficult.

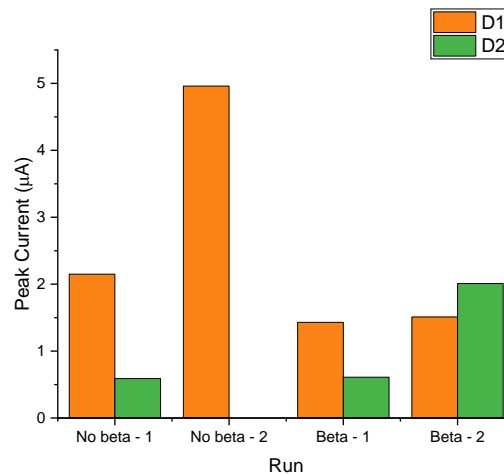


Figure 26: Bar chart comparing data of peak currents for D1 and D2.

In general, as can be seen in figure 26, that the threshold temperatures for D1 were considerably lower than for D2. The one exception is the beta – 1 run for D1 and the beta – 2 run for D2, where the latter is 5 °C lower.

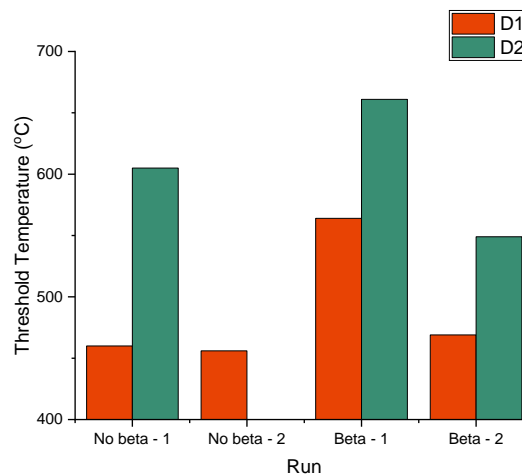


Figure 27: Comparison of the threshold temperatures for D1 and D2.

The data in figure 27, and somewhat figure 26, would suggest a slight preference for the thinner film having an enhanced thermionic emission relative to the thicker film. This would agree with the theory, that because D1 is considerably more nanocrystalline, with a vastly larger grain boundary density, electrons from the bulk can traverse to the surface with greater ease. In D2, these electrons are blocked by potential barriers in the bulk and cannot conduct to the surface.

3.2.3 Effect of Substrate on Thermionic Emission

Figure 28 shows the peak currents for Mo1 and D1, the 2 short growth films, displayed in an illustrative manner in a bar chart. There is a marked increase in peak emission with the molybdenum substrate relative to the diamond.

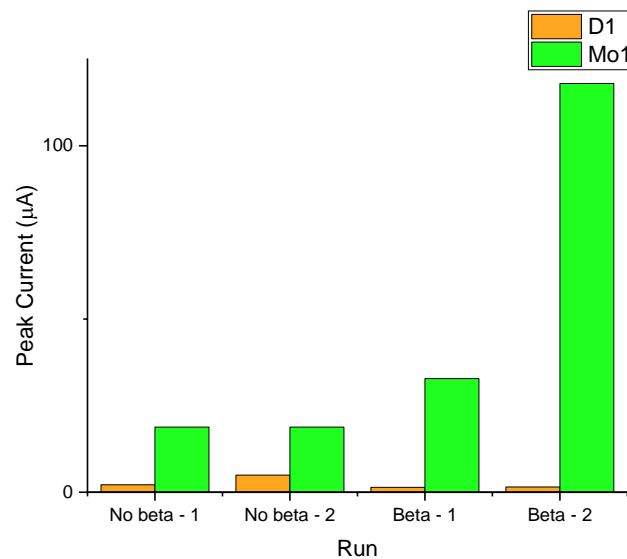


Figure 28: Peak emission currents plotted on a bar chart for Mo1 and D1.

Figure 29 shows the threshold temperatures compared for Mo1 and D1. Even though this result does not come out as anticipated, that being that threshold temperature you follow a similar trend to peak current, the comparison between the two isn't justified. Firstly, molybdenum and diamond both have very different optical properties and thus will be heated by the laser at varying rates. Secondly, both samples, when tested thermionically, used different emissivity's on the pyrometer. These emissivity's were not exact, and thus actual temperature may vary slightly between the samples. Finally, as previously discussed, and potentially most importantly, all but 1 of the runs for Mo1 had an issue with laser output fluctuations. All of these would have affected the temperature of the sample, the rate of heating, and therefore would have affected the threshold temperature.

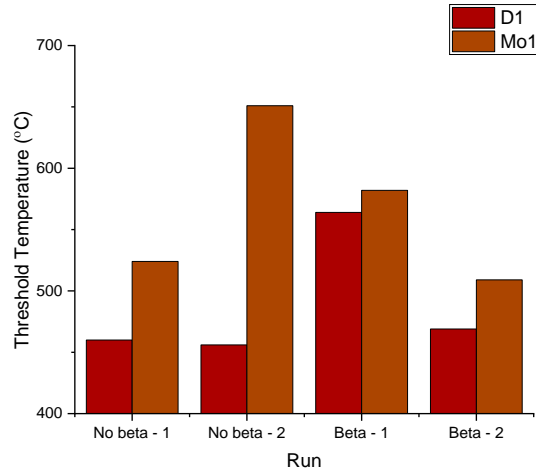


Figure 29: Threshold temperatures plotted on a bar chart for Mo1 and D1.

3.2.4 Observations on results and potential improvements to the method

As noted, previously, in writing this report there was a marked lack of results making it difficult to make clear deductions about beta enhancement of thermionic emission from CVD diamond. The reason for this was large due to the laboratory time allotted to do this experiment was being limited, and during this time the laboratory was out of order for a considerable time due to a broken air conditioning system.

Before discussing improvements to the method, it is useful to address the underlying theory of the Trap Passivation Effect (TPE). In a very disordered material, like nanocrystalline diamond, morphological defects, such as grain boundaries, can produce localised bands within the band gap [73]. In figure 30 the results of a Density Of States (DOS) calculation on nanocrystalline diamond are presented, where the dashed curve shows the bands for bulk carbon, and the solid curves show the bands for the grain boundary, where the π orbitals in the sp^2 hybridised carbon lie within the band gap [74]. At room temperature, the diamond films used in this project are reasonably resistive, and thus these holes remain unfilled. These traps will lead to a reduction in charge carrier mobility, thus reducing the conductivity [75]. After multiple runs, these electron traps will slowly be filled until they are all filled, and any subsequent electron excitation will be directly into the conduction band. This will, over a number of runs increase the thermionic output.

Therefore, to get a better picture of the thermionic properties of these samples, it would have been very informative to cycle each sample, from 300 – 600 °C, multiple times to see TPE in action. This would give a greater understanding of how the thermionic properties of these samples will evolve

with time, and also generated a greater number of data points which would have added more weight to the conclusions obtained from this project.

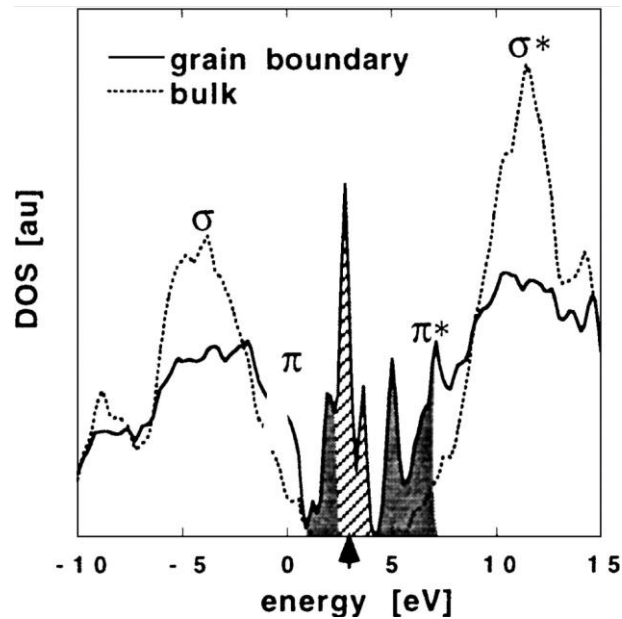


Figure 30: DOS calculation detailing the band states for bulk diamond (dashed curve) and grain boundary diamond (solid curve) ^[74].

It is also important to discuss the unpredictability and variability in the data. Certain samples, with runs under the exact same conditions, tended to give very different results. Detailed below are some potential origins for these differences and their likelihood has been discussed:

1. Over multiple runs the conductivity of each sample may have been changed via TPE. However, this effect seems to increase the thermionic emission only a small amount over a large amount of cycles. Also, this effect would have led to an increase per consecutive runs, so it is doubtful this plays a large part.
2. Inconsistency in the quality of the H-terminated surface at the time of the run. Slight differences in the H-termination conditions could have made a slight difference, however as conditions were extremely similar this is unlikely. Due to time constraints and equipment availability, often H-terminations were done in bulk, thus there may have been a slight delay from when the sample got H-terminated to when it was tested. This delay was a maximum of 4 days. It is assumed that this had an effect, however the scale of the reduction just by this process is difficult to judge.
3. Laser output fluctuations, as already mentioned, undoubtedly had an effect on the data for Mo1, however for the other two samples the pyrometer temperature accurately followed the set temperature ramp, so it's fair to say this had no effect on them.

4 Conclusion

Three polycrystalline nitrogen-doped diamond films were successfully grown using microwave plasma chemical vapour deposition, using gas composition of 4.2% methane in hydrogen and 2.4% nitrogen in methane. Two of the growths were done on 10×10 mm thermal grade diamond substrates, whereas one was grown on a 10×10 mm molybdenum substrate which was pre-seeded with micron scale diamond powder via manual abrasion. The growth periods were altered to vary the film thickness and morphology of the samples. The samples were characterized using Raman spectroscopy, with all samples showing the characteristic peak at 1332 cm^{-1} which confirmed the presence of diamond. Two of the samples showed a broad peak at $1400 - 1600 \text{ cm}^{-1}$, which was attributed to graphitic carbon. A morphological investigation was carried out on each sample using scanning electron microscopy. This showed that the two thin samples were considerably more nanocrystalline, with grain boundary lengths on the order of tens of nanometers. The thick film had much larger grain boundaries, on the order of tens of microns, with a much smoother surface.

The thermionic investigation into each sample was undertaken. Before each run, the samples were hydrogen terminated in a pure hydrogen plasma using microwave plasma chemical vapour deposition. For each run, the sample was radiatively heated using a CO_2 laser, from a start point of $300 \text{ }^\circ\text{C}$ to a maximum of $750 \text{ }^\circ\text{C}$ for around 30 seconds, and then the temperature was ramped down back to $300 \text{ }^\circ\text{C}$. During the run the current was measured from the emitted electrons from the sample to a collector, with a 25 V bias between them, with a gap of $200 \mu\text{m}$. Beta enhancement was also investigated, using an enclosed ^{63}Ni (28 MBq) 7×7 mm sample. The results showed a 1.42 – 3.47 – fold decrease for the diamond substrate short growth, the diamond substrate long growth showed a 1.07 – 3.41 – fold increase and the sample grown on molybdenum showed a 1.74 – 6.24 – fold increase., when irradiated by beta, however due to a lack of data this conclusion is very weak. In general, the thinner film grown on diamond showed a greater thermionic emission current, however there was variability in the results. The molybdenum substrate sample ubiquitously showed a greater thermionic emission current relative to the diamond grown sample.

The unpredictability of the results was discussed, including giving some possible origins of the variability and commenting on their likelihood. Improvements to the methods were provided.

5 Further Work

This section will detail topics of further work which could extend the ideas and theories which have been touched on in this work.

1. Creating an Air Stable Negative Electron Affinity

Over time, if kept in air, the hydrogen will become contaminated with moisture and the negative electron affinity will diminish, making it less, requiring it to be re-terminated. If kept in vacuum, the termination on the surface will last considerably longer, and potential surface contaminants can be controlled with the use of getters, yet this may not always be feasible and make storage difficult, and a more air stable surface termination would be preferable. Work has been done by K. O'Donnell *et al* on lithium-covered oxygen-terminated diamond, established an air stable negative electron affinity [76]. It would be very interesting to see the thermionic characteristics of such a terminated film, as this could lead to a much more robust material for use in diamond-based devices.

2. Forming a Schottky Emitter

A novel idea that is only recently gaining an interest and is currently under investigation by Bristol researchers is the formation of a Schottky emitter by a graphene layer on top of an NEA diamond surface. The formation of graphene on diamond has been done successfully before, either through graphitization of a diamond (111) surface [77] or grown by CVD on a metal substrate, often copper foil, and transferred to diamond [78]. Graphene is a considerably more conductive allotrope of diamond and testing the thermionic properties of such a material may yield very interesting results. Another application proposed for graphene on diamond is a solar blind UV detector [79].

3. Deuterium Termination

Testing the performance of D-terminated n-type diamond was originally planned to be a key part of this project but due to time constraints, it was not possible. The thermal instability of hydrogen-terminations is a large problem for high temperature devices and lessens the operational range. Deuterium-terminated surfaces should in theory yield a very similar NEA, which has been experimentally confirmed using ultraviolet photoemission spectroscopy [80]. Testing the thermionic properties, in particular how the work function varies with temperature, could yield a much more thermally stable emitter material capable of operation several hundred degrees high than for hydrogen.

6 Bibliography

- ¹ J. Robertson, *Diamond and Related Materials*, 1992, **1**, 397-406.
- ² M. Seal, *Materials Science and Engineering: B*, 1992, **11**, 167-171.
- ³ T. Anthony, *Vacuum*, 1990, **41**, 1356-1359.
- ⁴ D. D. L. Chung, *Journal of Materials Science*, 2002, **37**, 1475-1489.
- ⁵ F. Diederich and Y. Rubin, *Angewandte Chemie International Edition in English*, 1992, **31**, 1101-1123.
- ⁶ F. Maier, M. Riedel, B. Mantel, J. Ristein and L. Ley, *Physical Review Letters*, 2000, **85**, 3472-3475.
- ⁷ M. Seal, *Diamond and Related Materials*, 1992, **1**, 1075-1081.
- ⁸ F. Lenzini, N. Gruhler, N. Walter and W. Pernice, *Advanced Quantum Technologies*, 2018, **1**, 1800061.
- ⁹ I. Aharonovich, A. Greentree and S. Prawer, *Nature Photonics*, 2011, **5**, 397-405.
- ¹⁰ H. Tracy Hall, 1955.
- ¹¹ S. Eaton-Magaña, J. Shigley and C. Breeding, *Gems & Gemology*, 2017.
- ¹² W. G. Eversole, 1962.
- ¹³ M. Kamo, Y. Sato, S. Matsumoto and N. Setaka, *Journal of Crystal Growth*, 1983, **62**, 642-644.
- ¹⁴ J. Angus, *Diamond and Related Materials*, 2014, **49**, 77-86.
- ¹⁵ T. Anthony, *Vacuum*, 1990, **41**, 1356-1359.
- ¹⁶ W. Kulisch and C. Popov, *physica status solidi (a)*, 2006, **203**, 203-219.
- ¹⁷ R. Mendes de Barros, E. Corat, N. Ferreira, T. de Souza, V. Trava-Airoldi, N. Leite and K. Iha, *Diamond and Related Materials*, 1996, **5**, 1323-1332.
- ¹⁸ G. Ristić, Ž. Bogdanov, S. Zec, N. Romčević, Z. Dohčević-Mitrović and Š. Miljanić, *Materials Chemistry and Physics*, 2003, **80**, 529-536.
- ¹⁹ Y. Mankelevich and P. May, *Diamond and Related Materials*, 2008, **17**, 1021-1028.
- ²⁰ T. Lin, G. Yu, A. Wee, Z. Shen and K. Loh, *Applied Physics Letters*, 2000, **77**, 2692-2694.
- ²¹ A. Goyette, Y. Matsuda, L. Anderson and J. Lawler, *Journal of Vacuum Science & Technology A: Vacuum, Surfaces, and Films*, 1998, **16**, 337-340.
- ²² E. Mahoney, B. Truscott, M. Ashfold and Y. Mankelevich, *The Journal of Physical Chemistry A*, 2017, **121**, 2760-2772.
- ²³ S. Harris and A. Weiner, *Journal of Applied Physics*, 1994, **75**, 5026-5032.
- ²⁴ R. Kalish, *Carbon*, 1999, **37**, 781-785.
- ²⁵ G. Braunstein and R. Kalish, *Journal of Applied Physics*, 1983, **54**, 2106-2108.
- ²⁶ H. Kato, S. Yamasaki and H. Okushi, *Applied Physics Letters*, 2005, **86**, 222111.
- ²⁷ S. Bhattacharyya, O. Auciello, J. Birrell, J. Carlisle, L. Curtiss, A. Goyette, D. Gruen, A. Krauss, J. Schlueter, A. Sumant and P. Zapol, *Applied Physics Letters*, 2001, **79**, 1441-1443.
- ²⁸ K. Thonke, *Semiconductor Science and Technology*, 2003, **18**, S20-S26.
- ²⁹ R. Farrer, *Solid State Communications*, 1969, **7**, 685-688.
- ³⁰ L. Wang and A. Zunger, *Physical Review B*, 2002, **66**.
- ³¹ C. Bandis and B. Pate, *Physical Review Letters*, 1995, **74**, 777-780.
- ³² A. Hatta, K. Ogawa, N. Eimori, M. Deguchi, M. Kitabatake, T. Ito and A. Hiraki, *Applied Surface Science*, 1997, **117-118**, 592-596.
- ³³ A. Breskin, R. Chechik, E. Shefer, D. Bacon, Y. Avigal, R. Kalish and Y. Lifshitz, *Applied Physics Letters*, 1997, **70**, 3446-3448.
- ³⁴ P. May, J. Stone, M. Ashfold, K. Hallam, W. Wang and N. Fox, *Diamond and Related Materials*, 1998, **7**, 671-676.
- ³⁵ G. Wan, M. Cattelan and N. Fox, *The Journal of Physical Chemistry C*, 2019, **123**, 4168-4177.
- ³⁶ S. Lee, Z. Lin and X. Jiang, *Materials Science and Engineering: R: Reports*, 1999, **25**, 123-154.
- ³⁷ P. Baumann and R. Nemanich, *Surface Science*, 1998, **409**, 320-335.
- ³⁸ P. Fallon and L. Brown, *Diamond and Related Materials*, 1993, **2**, 1004-1011.

- ³⁹ O. Williams, M. Daenen, J. D'Haen, K. Haenen, J. Maes, V. Moshchalkov, M. Nesládek and D. Gruen, *Diamond and Related Materials*, 2006, **15**, 654-658. C. Wild, N. Herres and P. Koidl, *Journal of Applied Physics*, 1990, **68**, 973-978.
- ⁴⁰ C. Wild, N. Herres and P. Koidl, *Journal of Applied Physics*, 1990, **68**, 973-978.
- ⁴¹ F. Guthrie, *Proceedings of the Royal Society of London*, 1873, **21**, 168-169.
- ⁴² S. Halas, *Materials Science*, 2006, **24**.
- ⁴³ X. Wei, S. Wang, Q. Chen and L. Peng, *Scientific Reports*, 2014, **4**.
- ⁴⁴ C. Crowell, *Solid-State Electronics*, 1965, **8**, 395-399.
- ⁴⁵ J. Schwede, I. Bargatin, D. Riley, B. Hardin, S. Rosenthal, Y. Sun, F. Schmitt, P. Pianetta, R. Howe, Z. Shen and N. Melosh, *Nature Materials*, 2010, **9**, 762-767.
- ⁴⁶ A. Croot, G. Wan, A. Rowan, H. Andrade, J. Smith and N. Fox, *Frontiers in Mechanical Engineering*, 2017, **3**.
- ⁴⁷ J. Domenech-Garret, S. Tierno and L. Conde, *The European Physical Journal B*, 2013, **86**.
- ⁴⁸ K. Abdul Khalid, T. Leong and K. Mohamed, *IEEE Transactions on Electron Devices*, 2016, **63**, 2231-2241.
- ⁴⁹ W. Schlichter, *Annalen der Physik*, 1915, **352**, 573-640.
- ⁵⁰ W. Nottingham, G. Hatsopoulos and J. Kaye, *Journal of Applied Physics*, 1959, **30**, 440-441.
- ⁵¹ E. Gill, *The London, Edinburgh, and Dublin Philosophical Magazine and Journal of Science*, 1925, **49**, 993-1005.
- ⁵² J. Smith, G. Bilbro and R. Nemanich, *Diamond and Related Materials*, 2006, **15**, 2082-2085.
- ⁵³ J. Smith, G. Bilbro and R. Nemanich, *Journal of Vacuum Science & Technology B: Microelectronics and Nanometer Structures*, 2009, **27**, 1132.
- ⁵⁴ V. Chiplonkar and S. Desai, *Proceedings of the Indian Academy of Sciences - Section A*, 1966, **64**, 338-344.
- ⁵⁵ J. Houston, *Journal of Applied Physics*, 1959, **30**, 481-487.
- ⁵⁶ J. Lee, I. Bargatin, B. Vancil, T. Gwinn, R. Maboudian, N. Melosh and R. Howe, *Journal of Microelectromechanical Systems*, 2014, **23**, 1182-1187.
- ⁵⁷ P. May, *Endeavour*, 1995, **19**, 101-106.
- ⁵⁸ W. Paxton, M. Howell, W. Kang and J. Davidson, *Journal of Vacuum Science & Technology B, Nanotechnology and Microelectronics: Materials, Processing, Measurement, and Phenomena*, 2012, **30**, 021202.
- ⁵⁹ F. Koeck, R. Nemanich and J. Sharp, in *2013 26th International Vacuum Nanoelectronics Conference (IVNC)*, IEEE, 2013.
- ⁶⁰ J. Robertson, *Thin Solid Films*, 1997, **296**, 61-65.
- ⁶¹ D. Zhu, L. Zhang, R. Ruther and R. Hamers, *Nature Materials*, 2013, **12**, 836-841.
- ⁶² A. Ueda, Y. Nishibayashi and T. Imai, *Diamond and Related Materials*, 2009, **18**, 854-859.
- ⁶³ B. Truscott, M. Kelly, K. Potter, M. Johnson, M. Ashfold and Y. Mankelevich, *The Journal of Physical Chemistry A*, 2015, **119**, 12962-12976.
- ⁶⁴ B. Truscott, M. Kelly, K. Potter, M. Ashfold and Y. Mankelevich, *The Journal of Physical Chemistry A*, 2016, **120**, 8537-8549.
- ⁶⁵ V. Chatterjee, R. Harniman, P. May and P. Barhai, *Applied Physics Letters*, 2014, **104**, 171907.
- ⁶⁶ J. Lay, K. O'Donnell and P. May, *Chemical Physics Letters*, 2011, **515**, 151-154.
- ⁶⁷ P. Hidnert and W. Gero, *Scientific Papers of the Bureau of Standards*, 1924, **19**, 429.
- ⁶⁸ P. Jacobson and S. Stoupin, *Diamond and Related Materials*, 2019, **97**, 107469.
- ⁶⁹ U. Guler, A. Boltasseva and V. Shalaev, *Science*, 2014, **344**, 263-264.
- ⁷⁰ H. Dominguez-Andrade, A. Croot, G. Wan, J. Smith and N. Fox, *Review of Scientific Instruments*, 2019, **90**, 045110.
- T. Day, P. Hendra, A. Rest and A. Rowlands, *Spectrochimica Acta Part A: Molecular Spectroscopy*, 1991, **47**, 1251-1262.
- ⁷² R. BOWLING, R. PACKARD and R. MCCREERY, *ChemInform*, 1989, **20**.
- ⁷³ J. Dacuña and A. Salleo, *Physical Review B*, 2011, **84**.
- ⁷⁴ D. M. Gruen, *Annu. Rev. Mater. Sci.*, (1999), **29**, 211-259.
- ⁷⁵ J. Montero, J. Bisquert, G. Garcia-Belmonte, E. Barea and H. Bolink, *Organic Electronics*, 2009, **10**, 305-312.
- ⁷⁶ K. O'Donnell, M. Edmonds, J. Ristein, A. Tadich, L. Thomsen, Q. Wu, C. Pakes and L. Ley, *Advanced Functional Materials*, 2013, **23**, 5608-5614.
- ⁷⁷ N. Tokuda, M. Fukui, T. Makino, D. Takeuchi, S. Yamsaki and T. Inokuma, *Japanese Journal of Applied Physics*, 2013, **52**, 110121.
- ⁷⁸ Y. Wu, Y. Lin, A. Bol, K. Jenkins, F. Xia, D. Farmer, Y. Zhu and P. Avouris, *Nature*, 2011, **472**, 74-78.
- ⁷⁹ M. Wei, K. Yao, Y. Liu, C. Yang, X. Zang and L. Lin, *Small*, 2017, **13**, 1701328.
- ⁸⁰ P. Baumann and R. Nemanich, *Surface Science*, 1998, **409**, 320-335.